



# Massively parallel and time-resolved RNA sequencing in single cells with scNT-seq

Qi Qiu<sup>1,2,3,7</sup>, Peng Hu<sup>1,2,3,7</sup>, Xiaojie Qiu<sup>4,6</sup>, Kiya W. Govek<sup>1,5</sup>, Pablo G. Cámara<sup>1,5</sup> and Hao Wu<sup>1,2,3</sup>✉

**Single-cell RNA sequencing offers snapshots of whole transcriptomes but obscures the temporal RNA dynamics. Here we present single-cell metabolically labeled new RNA tagging sequencing (scNT-seq), a method for massively parallel analysis of newly transcribed and pre-existing mRNAs from the same cell. This droplet microfluidics-based method enables high-throughput chemical conversion on barcoded beads, efficiently marking newly transcribed mRNAs with T-to-C substitutions. Using scNT-seq, we jointly profiled new and old transcriptomes in ~55,000 single cells. These data revealed time-resolved transcription factor activities and cell-state trajectories at the single-cell level in response to neuronal activation. We further determined rates of RNA biogenesis and decay to uncover RNA regulatory strategies during stepwise conversion between pluripotent and rare totipotent two-cell embryo (2C)-like stem cell states. Finally, integrating scNT-seq with genetic perturbation identifies DNA methylcytosine dioxygenase as an epigenetic barrier into the 2C-like cell state. Time-resolved single-cell transcriptomic analysis thus opens new lines of inquiry regarding cell-type-specific RNA regulatory mechanisms.**

Dynamic changes in RNA levels are regulated by the interplay between RNA transcription, processing and degradation<sup>1,2</sup>. Understanding the mechanisms by which the transcriptome is regulated in functionally diverse cell types thus requires cell-type-specific measurements of the temporal dynamics of gene expression. Recent advances in single-cell RNA sequencing (scRNA-seq) are leading to a more complete understanding of heterogeneity in cell types and states<sup>3</sup>. However, standard scRNA-seq methods capture a mixture of newly transcribed ('new') and pre-existing ('old') RNAs without being able to temporally resolve RNA dynamics.

Commonly used approaches for distinguishing new from old RNAs within the same population of transcripts rely on RNA metabolic labeling that utilizes exogenous nucleoside analogs such as 4-thiouridine (4sU) and biochemical enrichment of labeled RNAs<sup>1</sup>. Although these methods have yielded critical insights into RNA dynamics regulation, they require ample starting material and present challenges for enrichment normalization. Several methods were recently developed to chemically convert 4sU into cytidine analogs, yielding uracil-to-cytosine substitutions that label newly transcribed RNAs after reverse transcription<sup>4–6</sup>. These chemical approaches permit direct measurement of temporal information about cellular RNAs without biochemical enrichment. Recent studies demonstrated the feasibility of jointly profiling new and old transcriptomes at single-cell levels by integrating Smart-seq/plate-based scRNA-seq with one of these chemical approaches such as thiol(SH)-linked alkylation for the metabolic sequencing of RNA (SLAM-seq)<sup>7,8</sup>. However, these Smart-seq/plate-based methods suffer from several limitations. First, they are costly and time consuming, thus prohibiting large-scale analysis of highly heterogeneous cell populations. Second, these methods lack unique molecular identifiers (UMIs), preventing accurate quantification of new transcript levels.

To overcome these constraints, we developed scNT-seq, a high-throughput and UMI-based scRNA-seq method that combines metabolic RNA labeling, droplet microfluidics and chemically

induced recoding of 4sU to a cytosine analog to simultaneously measure new and old transcriptomes from the same cell. We demonstrate that scNT-seq enables time-resolved analysis of cellular RNA dynamics, gene regulatory network (GRN) activity and cell-state trajectories at single-cell levels while it substantially improves the scalability and reduces the cost.

## Results

**Development and validation of scNT-seq.** To develop scNT-seq, we focused on the Drop-seq platform because its unique barcoded bead design affords immobilization of mRNAs for massively parallel on-bead chemical conversion reactions and UMI-based scRNA-seq analysis, and this droplet microfluidics platform is widely adopted<sup>9–13</sup>. The scNT-seq method consists of the following key steps (Fig. 1a): (1) metabolically labeling of cells with 4sU; (2–3) co-encapsulating individual cells with a barcoded oligo(dT) primer-coated bead in a nanoliter-scale droplet; (4) performing one-pot 4sU chemical conversion on pooled barcoded beads; (5–8) reverse transcription, cDNA amplification, tagmentation and indexing PCR; and (9) using a UMI-based statistical model to analyze T-to-C substitutions within transcripts and infer the new transcript fraction<sup>14</sup>.

To identify the optimal reaction conditions on barcoded beads, we explored two chemical approaches (SLAM-seq<sup>4</sup>: iodoacetamide (IAA)-based reaction; TimeLapse-seq<sup>5</sup>: 2,2,2-trifluoroethylamine (TFEA)/sodium periodate (NaIO<sub>4</sub>)-based reaction) and benchmarked their performance with species-mixing experiments using mouse embryonic stem cells (mESCs) and human K562 cells. TFEA/NaIO<sub>4</sub>-based chemistry substantially outperformed IAA-based chemistry in a one-pot chemical reaction on pooled beads (Fig. 1b). We noted that chemical treatment alone negatively affected the library complexity (genes/UMIs detected per cell; Extended Data Fig. 1a), but this issue could be overcome by using second-strand synthesis (2nd SS) to recover partially reversed transcribed mRNAs (see below). The collision rate was compara-

<sup>1</sup>Department of Genetics, University of Pennsylvania, Philadelphia, PA, USA. <sup>2</sup>Penn Epigenetics Institute, University of Pennsylvania, Philadelphia, PA, USA.

<sup>3</sup>Institute of Regenerative Medicine, University of Pennsylvania, Philadelphia, PA, USA. <sup>4</sup>Department of Cellular and Molecular Pharmacology, University of California, San Francisco, San Francisco, CA, USA. <sup>5</sup>Institute of Biomedical Informatics, University of Pennsylvania, Philadelphia, PA, USA. <sup>6</sup>Present address:

Whitehead Institute, Cambridge, MA, USA. <sup>7</sup>These authors contributed equally: Qi Qiu, Peng Hu. ✉e-mail: [haowu2@penncmedicine.upenn.edu](mailto:haowu2@penncmedicine.upenn.edu)

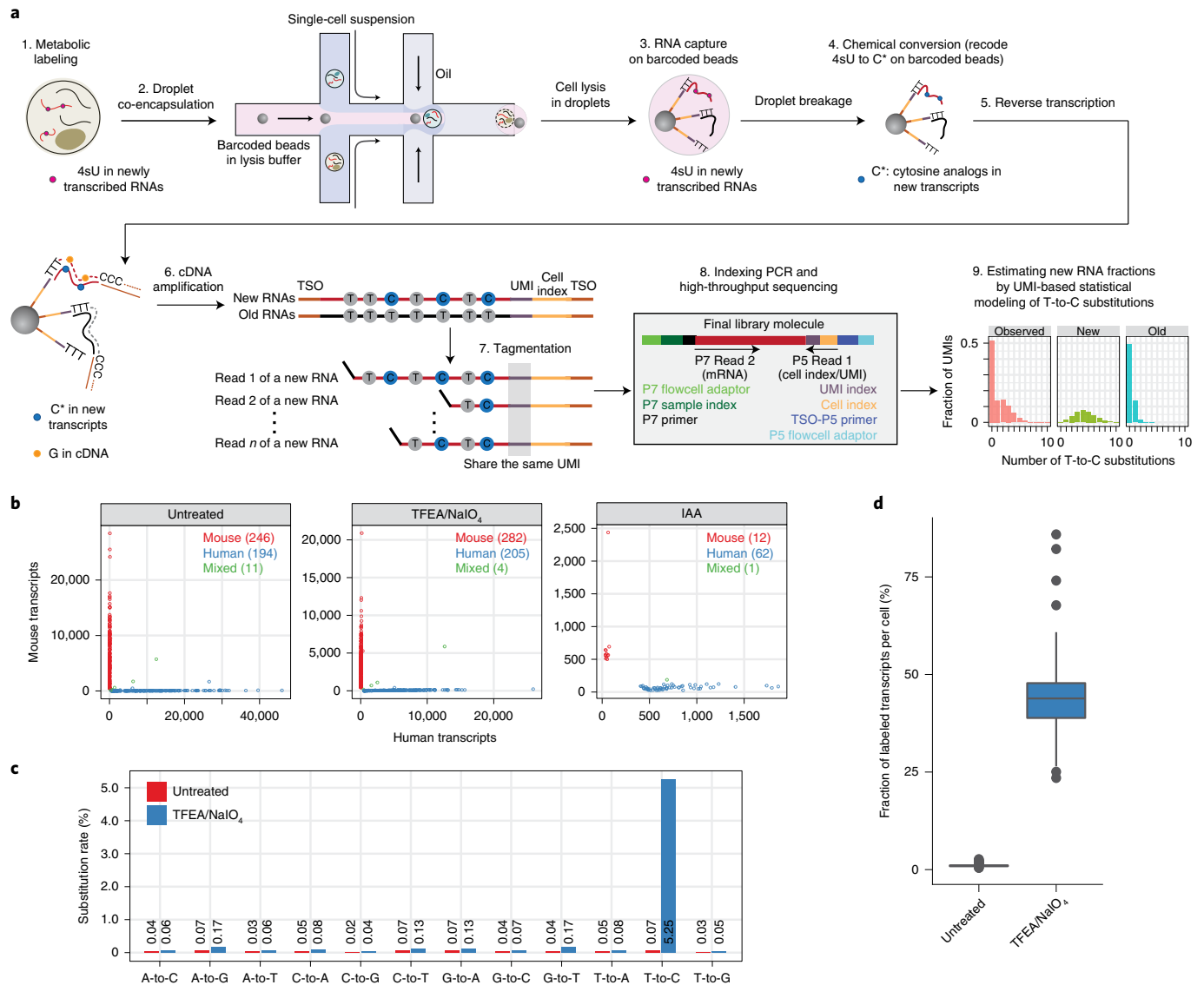


**Fig. 1 | Development and validation of scNT-seq. a**, Overview of scNT-seq. TSO, template switch oligo. **b**, Species-mixing experiment benchmarks the performance of TFEA/NaIO<sub>4</sub>- and IAA-based chemical conversion reactions on pooled beads in scNT-seq, by sequencing a mix (1:1) of human K562 cells and mESCs. The scatterplot shows the number of transcripts (UMIs) mapped to the mouse (y axis) or human (x axis) genome for each cell (dot) that is colored by its identity (human, blue; mouse, red; mixed, green). **c**, Bar plot showing nucleotide substitution rates in 4sU-labeled K562 cells. Untreated, control cells that were not chemically treated were used. **d**, Box plots showing the fraction of 4sU-labeled transcripts (UMI) per cell in untreated ( $n=193$  cells) and TFEA/NaIO<sub>4</sub>-treated ( $n=202$  cells) K562 cells. See ‘Data visualization’ in the Methods for definitions of box plot elements.

ble between TFEA/NaIO<sub>4</sub>-based scNT-seq and standard Drop-seq (Fig. 1b), demonstrating the specificity of scNT-seq in analyzing single-cell transcriptomes. As expected, 4sU labeling and TFEA/NaIO<sub>4</sub> treatment resulted in a specific increase in T-to-C substitution rate (Fig. 1c) and in the fraction of labeled transcripts at population and single-cell levels (Fig. 1d and Extended Data Fig. 1b). Moreover, scNT-seq worked efficiently with both freshly isolated and cryo-preserved cells (Extended Data Fig. 1c), and aggregated single-cell transcriptomes were highly correlated between biological replicates (Extended Data Fig. 1d). Collectively, these data demonstrate the feasibility of detecting metabolically labeled new transcripts at single-cell levels using a high-throughput droplet microfluidics platform.

**Evaluating scNT-seq performance for detecting activity-induced new RNAs.** Neuronal activity induces the expression of hundreds

of activity-regulated genes (ARGs) in the vertebrate brain, leading to new protein synthesis and epigenetic changes necessary for short- and long-term memories of experiences<sup>15</sup>. Recent studies suggest that different neuronal activity patterns could induce a distinct set of ARGs<sup>16</sup> that are highly cell-type specific *in vivo*<sup>10</sup>. The activity-induced gene expression program is well characterized for primary cortical neuronal cultures, which can serve as a model system for evaluating the performance of scNT-seq in quantifying new and old RNAs. We metabolically labeled primary mouse cortical cultures (200  $\mu$ M 4sU) for 2 h and stimulated the cells with different durations of neuronal activity (0, 15, 30, 60 and 120 min of potassium chloride (KCl)-mediated membrane depolarization; Extended Data Fig. 2a). After quality filtering, we retained 20,547 paired single-cell new and old transcriptomes (Fig. 2a, Extended Data Fig. 2b and Supplementary Table 1). We identified all major cell types expected in the embryonic mouse cortex: *Neurod6* + corti-

cal excitatory neurons (Ex, 68.5%), four *Gad1* + inhibitory neuronal subtypes (Inh1–4, 13.9% in total), *Dlx1/Dlx2* + inhibitory neuronal precursors (Inh-NP, 1.7%), two subpopulations of *Nes/Sox2* + excitatory neuronal precursors (Ex-NP1/2, 10.4% in total) and *Nes/Aldh1l1* + radial glial cells (RG, 5.5%; Fig. 2a and Extended Data Fig. 2b).

To evaluate scNT-seq for quantitatively distinguishing new from old RNAs and the extent of incomplete 4sU labeling of new transcripts<sup>7,17</sup>, we counted and statistically modeled T-to-C substitutions in UMI-linked transcripts (Methods). Compared to Smart-seq/plate-based methods that are constrained by the fixed read length, the coverage of uridines or T-to-C substitutions in each transcript was substantially improved in UMI-based scNT-seq analysis (Extended Data Fig. 3a,b). Analysis of both activity-induced genes (for example, *Fos*, new/total RNA ratio: 90.0%) and slow turnover housekeeping genes (for example, *Mapt*, new/total RNA ratio: 1.7%) in excitatory neurons suggests that our statistical correction model allows scNT-seq to accurately distinguish newly transcribed RNAs from pre-existing ones (Extended Data Fig. 3c–e).

Principal component analysis (PCA) of highly variable genes (HVGs) could completely separate activity-induced (120 min) from resting-state (0 min) excitatory neurons using either new RNAs or new-to-total RNA ratios (NTRs; Fig. 2b). Interestingly, PCA on total or old RNAs still partially separated resting and stimulated neurons (Fig. 2b), which may in part be due to the neuronal activity-regulated stability of some old RNAs. By contrast, non-neuronal cells (Ex-NP/RG) did not exhibit activity-dependent separation (Fig. 2b). Some ARGs, such as *Jun* and *Btg2*, were specifically induced in excitatory neurons, but other ARGs (for example, *Egr1*, *Fos* and *Npas4*) were broadly induced in many cell types, including non-neuronal cells, albeit with different magnitudes and response patterns (Fig. 2c, Extended Data Fig. 2c,d and Supplementary Table 2). There was little to no change at old RNA levels in response to activity (Fig. 2c). Thus, scNT-seq reveals cell-type-specific, activity-induced, immediate transcriptional changes.

**Identification of neuronal activity-induced, time-resolved regulon activity.** Regulon activity of a transcription factor (TF) can be quantified at single-cell resolution by linking *cis*-regulatory sequences to single-cell gene expression. Jointly profiling new and old transcriptomes by scNT-seq may enable parallel analysis of both dynamic regulons induced by external stimuli and stable regulons related to cellular identities. By applying single-cell regulatory network inference and clustering (SCENIC)<sup>18</sup> to paired single-cell new and old transcriptomes, we identified 79 co-regulated TF regulons with significant *cis*-regulatory motif enrichment in at least one cell type (Supplementary Table 3). Among them, 18 regulons showed significant changes in response to neuronal activity patterns (Fig. 2d). Many immediately early genes (IEGs) that are early-response ARGs encode TFs required for activating late-response ARGs<sup>15</sup>. With newly transcribed (but not pre-existing) RNAs, SCENIC analysis revealed an activity-dependent increase in regulon activity of both IEG TFs (for example, *Fos* and *Jun*) and constitutively expressed TFs (for example, *Srf* and *Mef2*) that are post-translationally activated<sup>15</sup> (Fig. 2d). Regulon activity of these TFs (for example, *Jun*) was specifically detected in neurons (Fig. 2d,e). Interestingly, we also identified several activity-induced TFs not previously implicated in neuronal activation (Fig. 2d). For example, *Maff*, as a small MAF family protein lacking the transactivation domain<sup>19</sup>, is associated with both activity-dependent (mainly with new RNAs) and activity-independent regulon activities (Fig. 2e). Interestingly, target genes of *Maff* significantly overlap with those of the IEG TF *Fosb* (Extended Data Fig. 2e), and gene ontology (GO) analysis suggests that *Maff* targets are functionally related to neuron projection ( $P=6.47 \times 10^{-7}$ ) and synapse ( $P=2.30 \times 10^{-3}$ ). In addition, we found that activity-independent TF regulons are often cell-type

specific (for example, *Neurod1/2* for Ex and *Dlx1/2* for Inh) and are associated with both new and old RNAs (Fig. 2d). Thus, scNT-seq can reveal temporal dynamics of cell-type-specific TF regulon activities at single-cell resolution.

**Metabolic labeling-based time-resolved RNA velocity analysis.** Recent work showed that the time derivative of gene expression, termed ‘RNA velocity’, can be estimated by distinguishing unspliced (intronic reads) from spliced (exonic reads) mRNAs in scRNA-seq datasets and used to inform how transcriptional states in single cells change over time (on the scale of hours)<sup>20</sup>. We first examined whether RNA velocity analysis can predict the transcriptional state trajectory of individual cells in response to brief (minutes) and sustained (hours) neuronal activation. To this end, we focused on the excitatory neurons, as these cells robustly respond to neuronal activation. However, no neuronal activity-dependent directionality was consistently detected in the splicing RNA velocity flow, irrespective of using all excitatory neurons (Extended Data Fig. 4a) or only high-quality cells (Fig. 3a). This is probably due to the sparsity of unspliced transcripts from many activity-induced genes that contain few introns and/or are of fast splicing kinetics (for example, *Egr1* and *Fos*; Extended Data Fig. 5a).

Because metabolic labeling can capture rapid changes in RNA levels<sup>21</sup> and detection of new RNAs via 3'-tagged UMIs is largely independent of gene structures, we reasoned that single-cell paired measurements of new and total RNAs from scNT-seq can be used to compute metabolic labeling-based RNA velocity that is scaled to labeling time (molecules per unit time). To quantify this time-resolved RNA velocity, we utilized dynamo<sup>22</sup>, a computational method that explicitly models metabolic labeling-based scRNA-seq. Phase portraits of early- (*Egr1* and *Fos*) and late- (for example, *Homer1*) response genes showed the expected deviations from the predicted steady-state relationship (Extended Data Fig. 5b). Measured by velocity flows (indicative of the observed and extrapolated cell states) in the low-dimensional embedding, metabolic labeling-based RNA velocity accurately recapitulated the transcriptional dynamics of neuronal activation, including a general movement of resting-state neurons (0 min) toward activated neurons (first phase) and second-phase movement from briefly stimulated cells (15–30 min) to longer stimulation (60–120 min; Fig. 3a and Extended Data Fig. 4a). Furthermore, randomized velocity controls support the specificity of the observed time-resolved RNA velocity flow (Fig. 3a and Extended Data Fig. 4a).

The two distinct phases of observed RNA velocity flows correlate with early- and late-response gene expression, respectively (Fig. 3b and Extended Data Figs. 4b and 6). We further identified activity-regulated TF regulons that were significantly enriched for early- ( $n=24$ ) or late- ( $n=73$ ) response genes (Fig. 3c and Extended Data Fig. 2d). We calculated the regulon activity of these activity-regulated TFs in each cell, based on the newly transcribed RNA levels of its target genes. By projecting regulon activity of these TFs onto the same embedding of velocity analysis, we constructed a single-cell resolution, time-resolved regulon activity map for a distinct class of TFs: early response (*Jun*) versus late response (*Mef2d* and *Maff*; Fig. 3d and Extended Data Fig. 4c). Thus, scNT-seq supports metabolic labeling-based, time-resolved RNA velocity analysis of dynamic cellular processes.

**scNT-seq reveals distinct RNA regulatory strategies during stem cell-state transition.** Determining RNA regulatory strategies in rare, transient cell populations is critical to understanding cell-state transition but remains a challenge. Cultured mESCs are derived from the inner cell mass of preimplantation blastocysts and exhibit a high level of transcriptional heterogeneity<sup>23</sup>. Interestingly, cells resembling totipotent 2C-stage embryos arise spontaneously in mESC cultures<sup>24</sup>, but 2C-like cells are rare (<1% in standard condi-

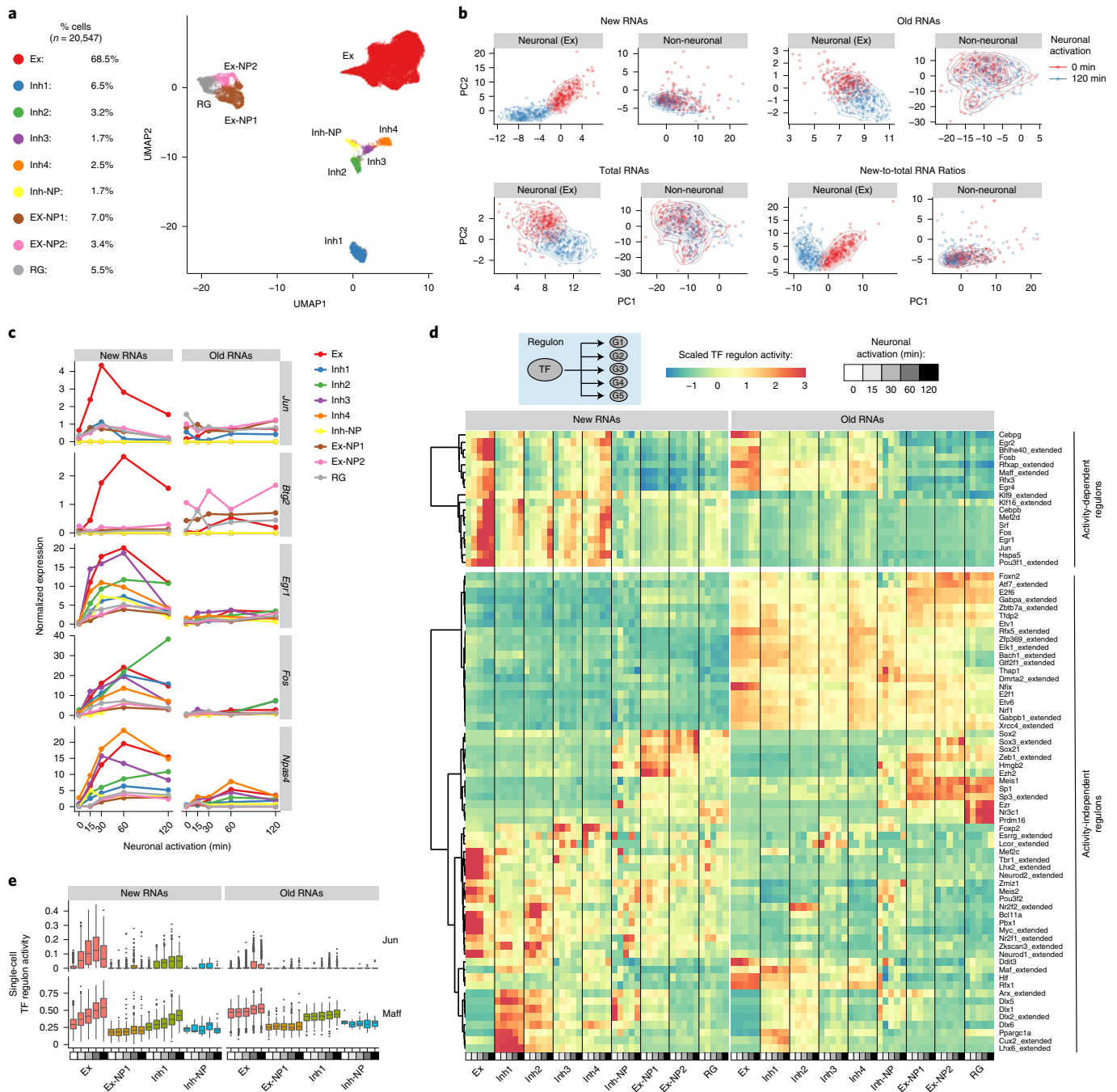


**Fig. 2 | scNT-seq captures newly synthesized transcriptomes and time-resolved regulon activity in response to neuronal activation. a**, UMAP visualization of 20,547 mouse cortical cells colored by their cell types. Fractions of each cell type are shown on the left. Ex, excitatory neurons; Inh, inhibitory neurons; NP, neural progenitors; RG, radial glial cells. **b**, PCA plots showing excitatory neurons and non-neuronal cells at resting (0 min, red) or stimulated (120 min, blue) states based on their newly synthesized transcriptomes (new RNAs), pre-existing transcriptomes (old RNAs), whole transcriptomes (total RNAs) and NTRs. In total, 200 cells (>1,000 genes detected per cell) were randomly chosen from excitatory neurons or non-neuronal cells (Ex-NP1, Ex-NP2 and RG) at the two time points. Density of dots is indicated by contour lines. **c**, Line plot showing cell-type specific new and old RNA expression for select activity-induced genes in response to distinct activation durations. The mean new and old RNA levels were scaled by library size (TP10K, transcripts per 10,000 transcript/UMI counts). **d**, Clustered heat map showing cell-type-specific regulon activity of 79 TFs in response to neuronal activation, concurrently inferred from either new or old RNAs. A total of 18 activity-dependent regulons were associated with significantly increased new RNA levels of their target genes in at least one cell type (adjusted  $P < 0.05$  and fold change  $> 1.5$ ) after KCl stimulation. A two-sided Wilcoxon rank-sum test was used to assess the significance of the difference.  $P$  values were adjusted by Bonferroni correction.  $P$  values and regulon activity of each TF are available as source data and in Supplementary Table 3, respectively. **e**, Box plots showing cell-type-specific regulon activity (inferred from either new or old RNAs) of Jun and Maff in response to neuronal activation. Cell number, Ex:  $n = 1,422$  (0 min), 2,678 (15 min), 2,884 (30 min), 4,664 (60 min) and 1,863 (120 min); Ex-NP:  $n = 147$  (0 min), 169 (15 min), 218 (30 min), 391 (60 min) and 177 (120 min); Inh1:  $n = 146$  (0 min), 244 (15 min), 311 (30 min), 428 (60 min) and 166 (120 min); Inh-NP:  $n = 7$  (0 min), 3 (15 min), 12 (30 min), 20 (60 min) and 19 (120 min). See 'Data visualization' in the Methods for definitions of box plot elements.

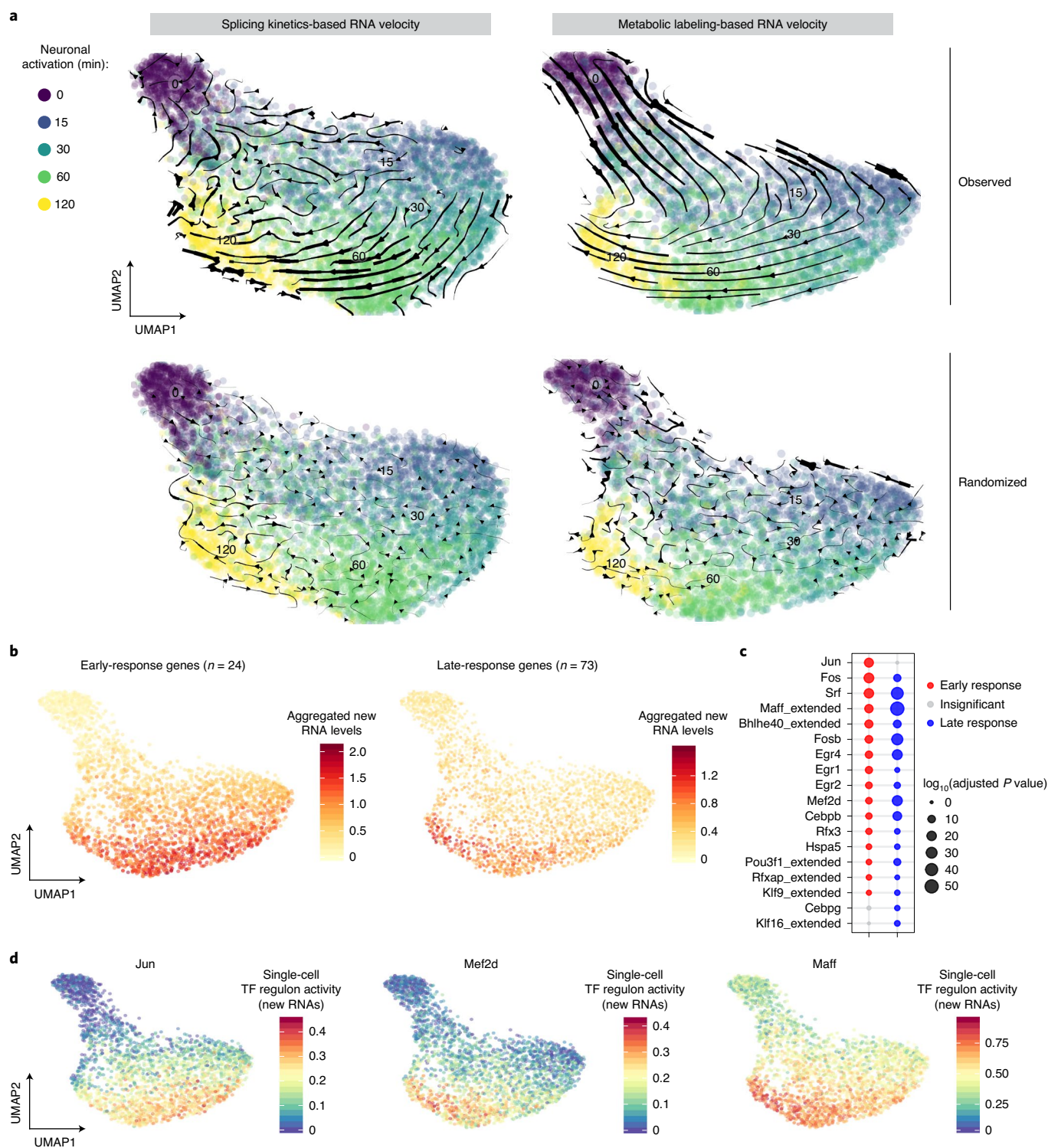


**Fig. 3 | Metabolic labeling-based RNA velocity analysis of rapid changes in transcriptional states.** **a**, UMAP visualization of excitatory neurons ( $n = 3,066$  cells,  $>2,000$  genes detected per cell) that were characterized by standard splicing kinetics-based (left) or metabolic labeling-based (right) RNA velocity analyses. Cells are color coded by time points. The streamlines indicate the integration paths that connect local projections from the observed state to the extrapolated future state. The lower UMAP plots (same as upper) show randomized velocity controls for splicing kinetics- or metabolic labeling-based RNA velocity. The streamline thickness indicates the magnitude of the velocity. **b**, UMAP visualization (same as right plot in **a**) of excitatory neurons colored by the average new RNA expression level (natural log transformation (TP10K + 1)) of 24 early- (left) or 73 late- (right) response genes. **c**, Dot plot showing enrichment of 24 early- or 73 late-response genes in activity-dependent TF regulon targets from all excitatory neurons ( $n = 13,511$  cells,  $>500$  genes detected per cell). The predicted regulon target genes were used as background for calculating statistical significance. The significance of enrichment is determined by a two-sided Fisher's exact test. The size of dots is scaled by  $-\log_{10}$ (false discovery rate (FDR)-adjusted  $P$  value), and significant regulons (adjusted  $P < 0.05$ ) are color coded for early- (red) or late- (blue) response genes.  $P$  values are available as source data. **d**, UMAP (same as right of **a**) showing excitatory neurons colored by the regulon activity of three representative TFs (Jun, Mef2d and Maff).

tions)<sup>24</sup>. Recent scRNA-seq studies revealed changes in total RNAs during the transition from the pluripotent to totipotent 2C-like state and identified an intermediate state during the transition<sup>25,26</sup>. It remains unclear how regulation of RNA synthesis and degradation contributes to the stepwise conversion between pluripotent and 2C-like states.

To capture rare 2C-like cells without using transgene induction<sup>26</sup> or fluorescent reporter lines<sup>24</sup>, wild-type (WT) mESCs were metabolically labeled with 4sU for 4 h and were subjected to scNT-seq analysis. After quality filtering, we obtained 4,633 single-cell transcriptomes from two biological replicates (Extended Data Fig. 7a,b). Besides mouse feeder cells (*Col1a2* and *Fbln2*), scNT-seq also identified all three principal states (pluripotent, 98.3%; intermediate, 1.0%; totipotent 2C-like, 0.7%) in mESCs using state-specific marker genes (Extended Data Fig. 7c, d). The percentage of rare 2C-like cells is consistent with previous reports<sup>24,27</sup>. As expected, many state-specific genes with regulatory functions (for example, *Zscan4d*) are associated with a higher proportion of new transcripts than those of housekeeping genes (for example, *Gapdh*; Extended Data Fig. 7e).

Next, we combined a pulse-chase strategy with scNT-seq to determine state-specific mRNA degradation rates (Fig. 4a). After removing partially differentiated cells (0.6% of all cells), we retained 20,059 stem cells from seven time points (Fig. 4b). We calculated the half-life of mRNAs in each cell state by computing the proportion of labeled transcripts for each gene at every time point and fitting a single exponential decay model. Consistent with bulk assay results<sup>4</sup>, we observed a substantial accumulation of T-to-C substitutions after 24 h of metabolic labeling and subsequent decrease to baseline after chase (Fig. 4c and Extended Data Fig. 8a). The RNA half-life determined by pulse-chase scNT-seq is concordant with those derived from bulk SLAM-seq assays<sup>4</sup> (Pearson's  $r=0.83$ ; Fig. 4d). Interestingly, RNA half-life estimated from one time-point labeling experiment<sup>28</sup> was less correlated with measurements from bulk assays (Pearson's  $r=0.51$ ; Fig. 4d). Furthermore, the top 10% most stable and unstable transcripts were enriched for similar GO terms that were uncovered by bulk SLAM-seq assays<sup>4</sup> (Extended Data Fig. 8b). Finally, we analyzed 2,616 commonly detected genes between cell states to reveal state-specific regulation of mRNA stability (Extended Data Fig. 8c,d and Supplementary Table 4). Thus, scNT-seq enables transcriptome-wide measurement of RNA stability in rare cell populations.

Using data from the one time-point labeling (Extended Data Fig. 7a) and pulse-chase (Fig. 4b) experiments, we computed the RNA synthesis and degradation rates in all three stem cell states (Methods). Next, we performed clustering of the synthesis rates, degradation rate constants and total RNA levels of 445 genes that exhibited high expression variability between states (Fig. 4e and Supplementary Table 5). By computing the similarity between synthesis and degradation dynamics<sup>29</sup>, we identified three major RNA regulatory strategies during the stepwise pluripotent-to-2C transition: cooperative (110 genes; negative similarity between RNA biogenesis and degradation dynamics), neutral (136 genes; small relative changes in RNA degradation rate compared with the synthesis rate) and destabilizing (199 genes; simultaneous increase or decrease of the synthesis

rate and the degradation rate). Further analysis indicated that genes with similar cellular functions may be controlled by similar RNA regulatory strategies. For instance, among the genes with destabilizing regulatory strategies, we identified functional enrichment for mRNA splicing (adjusted  $P=1.1\times 10^{-9}$ ), transcription regulation (adjusted  $P=3.9\times 10^{-5}$ ) and nucleosome assembly (adjusted  $P=9.8\times 10^{-3}$ ). Interestingly, even among the same subset of genes that follow destabilizing strategies and are downregulated in 2C-like states compared with the pluripotent state, total RNA dynamics of *Tet1* (Pearson's  $r=0.99$ ) and *Lefty2* (Pearson's  $r=0.95$ ) were preferentially regulated by changes in the RNA synthesis rate and the degradation rate, respectively (Fig. 4e and Supplementary Table 5). These results demonstrate that changes in both RNA synthesis and degradation contribute to gene expression dynamics during stem cell-state transitions.

**Time-resolved regulon analysis reveals TET-mediated regulation of the pluripotent-to-2C transition.** For many genes differentially expressed between pluripotent and 2C-like states (for example, *Ncl*, *Tet1* and *Zfp42*), their new RNA levels exhibited a more pronounced difference than that of old or total RNAs (Extended Data Fig. 9a). GO enrichment analysis further revealed that new RNAs are more robust than old or total RNAs to uncover certain state-specific biological processes such as 'protein deubiquitination' and related genes (for example, *Usp17lc*, *Usp17ld* and *Usp17le*; Extended Data Fig. 9a,b). These results support the observation that changes in RNA synthesis rates drive the RNA dynamics of many state-specific genes during the state transition (Fig. 4e).

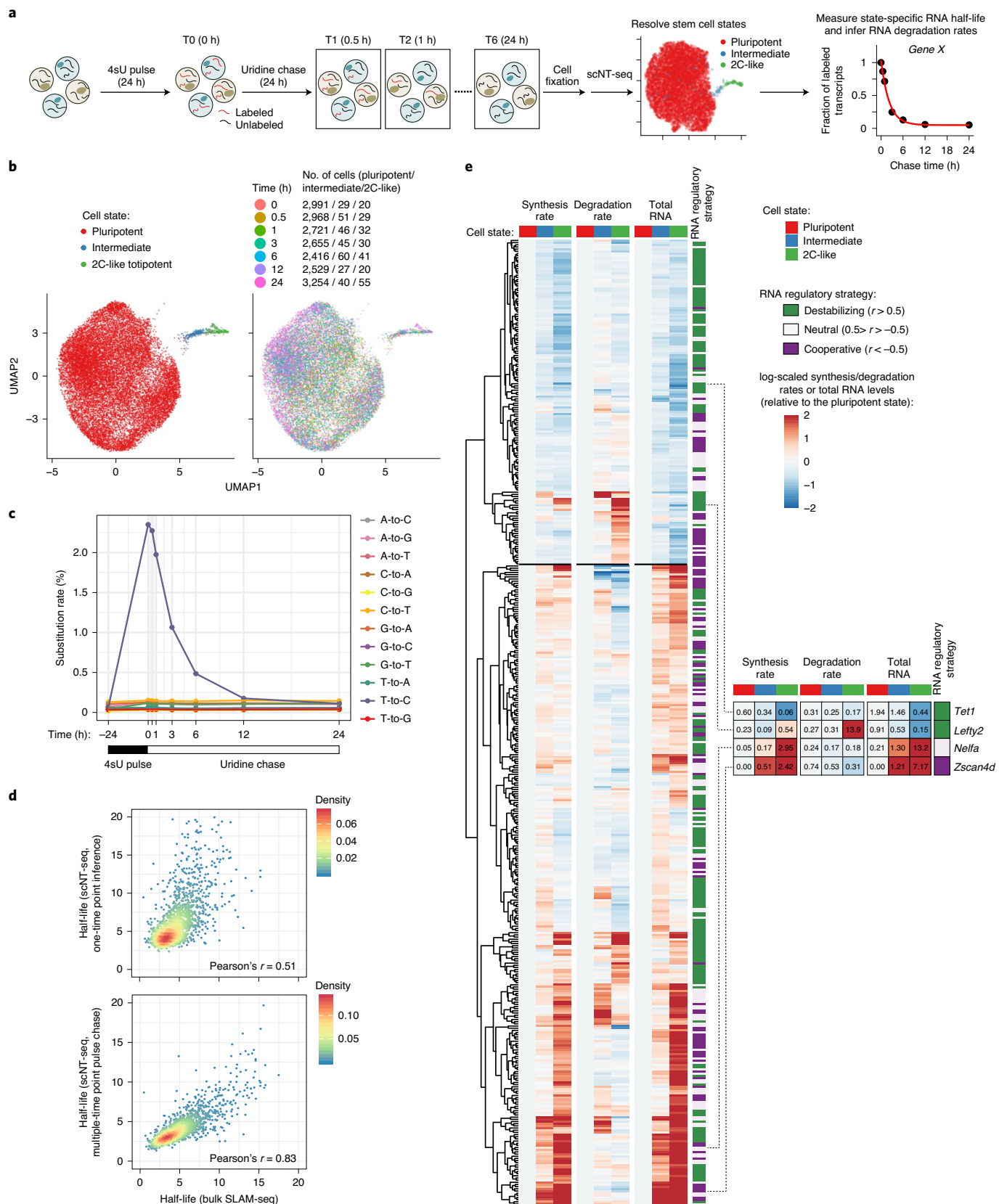
To further investigate transcriptional regulators underlying the control of RNA synthesis during the pluripotent-to-2C transition, we applied single-cell regulon analysis to both new and old transcriptomes (Fig. 5a). Because new RNAs exhibited more rapid changes than old RNAs (Fig. 5b) and aggregated new RNA levels of a TF's target genes provides a more direct measurement for its regulon activity, we focused our analysis on TFs or epigenetic regulators that show state-specific 'new RNA' regulon activity (Fig. 5c). In addition to well-established TFs related to pluripotency (for example, *Myc/Max* and *Nanog*) and cell-cycle regulation (for example, *E2f3* and *E2f5*), several epigenetic regulators were associated with a marked decrease in new RNA regulon activity during the pluripotent-to-2C transition (Fig. 5c). The TET family of DNA dioxygenases (*Tet1–3*) is of particular interest, as these epigenetic enzymes mediate active DNA demethylation at *cis*-regulatory elements and are known to play critical roles in maintaining mESC pluripotency<sup>30,31</sup>. During the transition from the pluripotent to 2C-like state, both new RNA level and regulon activity of *Tet1* rapidly decreased (Fig. 5b,c). The new RNA level of *Tet2* also decreased in both intermediate and 2C-like states, while *Tet3* was nearly undetected in all three states (Extended Data Fig. 9c).

To better understand how TET enzymes regulate cell-state transition, we generated mESCs deficient for all three Tet proteins (*Tet1*, *Tet2* and *Tet3* triple knockout; *Tet*-TKO) via CRISPR-Cas9 genome editing<sup>32</sup> and analyzed isogenic WT and *Tet*-TKO mESCs in parallel using scNT-seq (Extended Data Fig. 9d). While WT and mutant cells were intermingled in intermediate and 2C-like states, they

**Fig. 4 | scNT-seq reveals mRNA regulatory strategies during stem cell-state transition.** **a**, Design of pulse-chase scNT-seq experiments. **b**, UMAP visualization of 20,059 mESCs colored by three stem cell states (left) or by seven time points during chase (right). Cell numbers for each state across seven time points are also shown. **c**, Line plots showing changes in nucleotide substitution rates across seven time points of pulse chase. **d**, Scatterplots showing Pearson's correlation of RNA half-life measurements ( $n=1,926$  genes) between this study (top: one time-point inference (4sU, 4 h); bottom: multiple time-point pulse chase) and bulk SLAM-seq<sup>4</sup> in mESCs. **e**, Clustered heat maps of estimated synthesis rates (left), degradation rates (middle) and observed total RNA levels (right) of 445 genes across three stem cell states. The values in intermediate or 2C-like states were normalized to the pluripotent state. Also shown are RNA regulatory strategies (cooperative, 110 genes; neutral, 136 genes; destabilizing, 199 genes) color coded by similarity between the synthesis and degradation rates. Right, four representative genes with their raw synthesis and degradation rates and total RNA levels are indicated. The synthesis rate, degradation rate, total RNA abundance and regulatory strategy of each gene are shown in Supplementary Table 5.

were separately clustered by both genotypes and cell-cycle states within the pluripotent state (Fig. 5d and Extended Data Fig. 9e). Compared to WT cells, substantially more *Tet*-TKO cells in the pluripotent state were found proximal to the intermediate and 2C-like

states in the uniform manifold approximation and projection (UMAP; Fig. 5d), suggesting that *Tet*-TKO cells are more poised to transition to intermediate and 2C-like states. Consistent with a previous study<sup>27</sup>, *Tet*-TKO cells exhibited a marked increase in the



2C-like state (3.6 fold) compared to WT cells (Fig. 5e). Interestingly, *Tet*-TKO cells also showed a 2.2-fold increase in the intermediate state, suggesting that Tet enzymes act as regulators in the early stage of pluripotent-to-2C transition.

A recent study showed that Myc negatively regulates the transition toward intermediate and 2C-like states by actively maintaining the pluripotent transcriptome<sup>26</sup>. Because Tet1 regulon activity dynamics is similar to that of Myc/Max (Fig. 5c) and Tet1 targets are significantly overlapped with Myc/Max targets (Extended Data Fig. 9f), we asked whether Tet1 inhibits the pluripotent-to-2C transition through a similar mechanism. First, Tet1 regulon targets were significantly overlapped with pluripotent state-enriched newly transcribed RNAs ( $P = 1.36 \times 10^{-129}$ ) but not with 2C-like state-enriched new RNAs ( $P = 0.94$ ). Second, differential gene expression analysis identified 2,281 genes upregulated and 205 genes downregulated in the *Tet*-TKO pluripotent state (Fig. 5f and Supplementary Table 6), but very few genes were dysregulated in intermediate and 2C-like states in the absence of TET proteins. Finally, Tet1 direct targets were significantly enriched for downregulated genes ( $P = 1.29 \times 10^{-30}$ ) but less so for genes upregulated ( $P = 6.32 \times 10^{-3}$ ) in *Tet*-TKO mESCs, suggesting that TET proteins may maintain expression of their target genes functionally related to the pluripotent state. Indeed, GO analysis showed that genes downregulated in *Tet*-TKO mESCs were enriched for pluripotent state-specific biological processes (Fig. 5g). Collectively, Tet proteins may act as an epigenetic barrier for the transition from pluripotent to intermediate and 2C-like states by maintaining a pluripotent state-specific transcriptome.

**Second-strand synthesis reaction substantially enhances the efficiency of scNT-seq.** We reasoned that TFEA/NaIO<sub>4</sub> treatment may increase the failure rate of generating full-length cDNAs ('truncated' cDNAs in Fig. 6a), which is required for the 'template-switching' reaction to add the second PCR handle for cDNA amplification (step 6 in Fig. 1a). Indeed, the generation of truncated cDNA during reverse transcription could be a major reason leading to lower library complexity in scRNA-seq methods using the on-bead template-switching reaction<sup>33</sup>.

To improve scNT-seq performance for 3'-tagged new transcript counting analysis, we developed a random-primed second-strand synthesis (2nd SS) reaction to recover truncated cDNA (Fig. 6a) and benchmarked the performance of this approach in human K562 cells. The 2nd SS reaction in scNT-seq (4sU/TFEA/2nd SS) was compatible with the analysis of T-to-C substitution (Extended Data Fig. 10a) and led to a 2.2-fold increase in the number of genes and a 4-fold increase in the number of UMIs detected per cell, when compared to the standard scNT-seq protocol (4sU/TFEA) at matched sequencing depths (Fig. 6b). Further comparisons indicated that the new and old RNA levels and NTRs from the 2nd SS scNT-seq protocol were highly concordant with those derived from the standard protocol (Fig. 6c).

Next, we validated the 2nd SS scNT-seq protocol in analyzing cell-cycle-state-specific genes in K562 cells. All three experimental protocols (Drop-seq control: 4sU/2nd SS; scNT-seq: 4sU/TFEA or 4sU/TFEA/2nd SS) readily revealed major cell-cycle phases

using PCA (Fig. 6d and Extended Data Fig. 10b). While the levels of new RNAs, old RNAs and NTRs were generally comparable between standard and 2nd SS scNT-seq protocols (Extended Data Fig. 10c,d), 2nd SS scNT-seq increased the detection sensitivity for many genes (for example, *MKI67* in S phase and *CENPE* in G2M phase; Extended Data Fig. 10c,d), which is consistent with increased library complexity in 2nd SS scNT-seq datasets.

## Discussion

By combining TimeLapse chemistry with a high-throughput droplet microfluidics platform, scNT-seq enables joint profiling of newly synthesized and pre-existing transcriptomes of the same cell, capturing temporal information about mRNA at single-cell levels. Standard RNA velocity analysis uses endogenous RNA splicing kinetics to inform on the future trajectory of a cell; thus, it is limited by uncontrolled timing of RNA splicing and the sparsity of intronic reads for many genes. Because the timing and length of metabolic labeling periods can be experimentally controlled, direct counting of new and old transcripts via 3'-tagged UMIs in scNT-seq provides an unbiased means to calculate RNA kinetics parameters for all detectable genes. Using computational models that explicitly incorporate metabolic labeling-based single-cell measurements<sup>22</sup>, we could compute time-resolved RNA velocity for highly dynamic processes (minutes to hours). Furthermore, measuring new RNA levels of target genes linked to a TF can temporally resolve TF regulon activity at single-cell levels during external stimulation or cell-state transitions. Finally, with pulse-chase experiments, scNT-seq can more accurately estimate RNA kinetics parameters, revealing RNA regulatory strategies in rare cell populations.

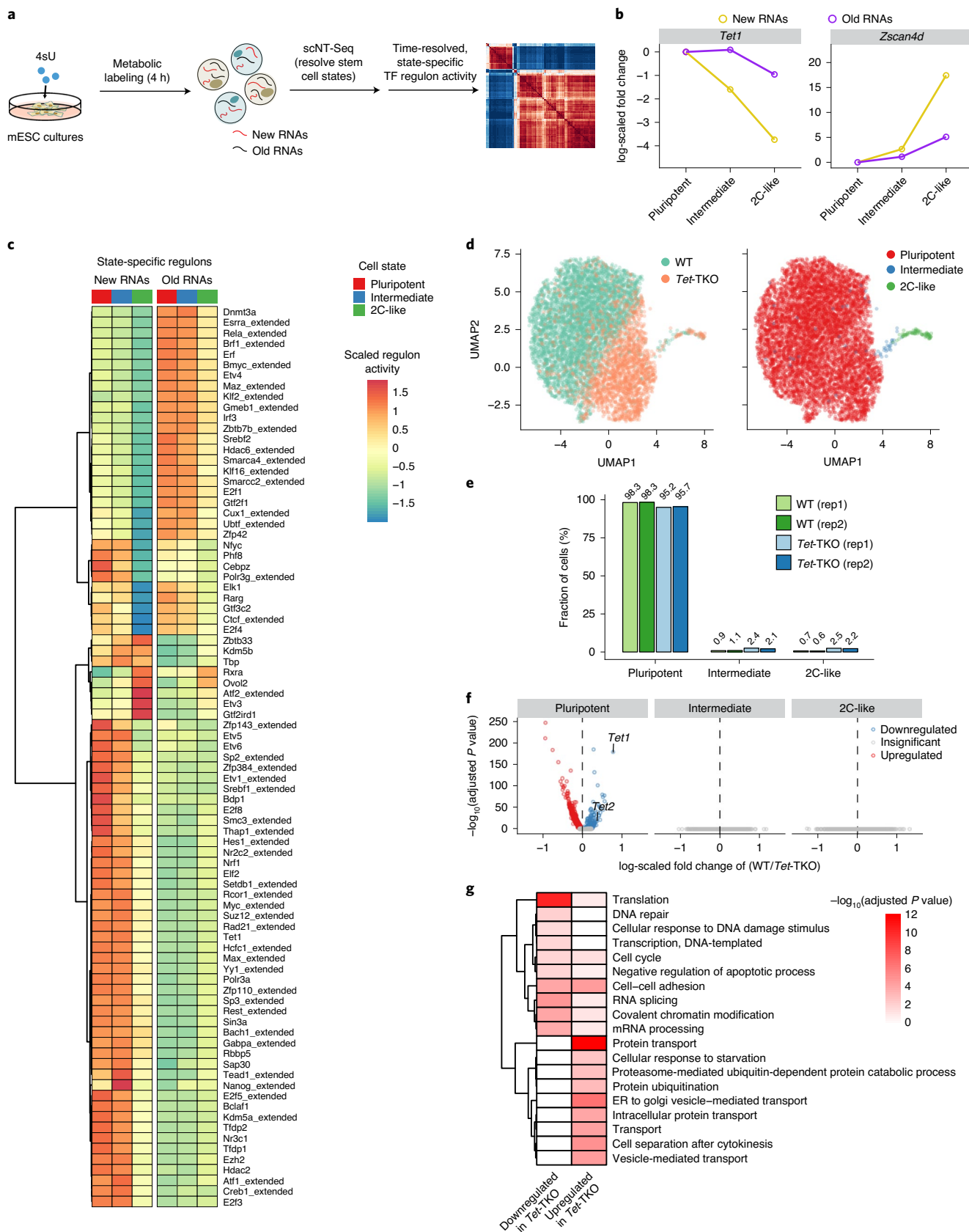
scNT-seq is conceptually similar to sci-fate<sup>34</sup>, a method that integrates single-cell combinatorial indexing with SLAM-seq chemistry, and was reported during the revision of this manuscript. Both methods share several technical advantages over SMART-seq/plate-based methods such as scSLAM-seq<sup>7</sup> and NASC-seq<sup>8</sup> (Supplementary Table 7). First, when combined with 2nd SS reactions, scNT-seq detects ~6,000 genes and ~20,000 UMIs per cell with a sequencing depth of ~50,000 reads per cell. This is comparable to the performance of sci-fate (~6,500 genes and ~26,000 UMIs per cell with ~200,000 reads per cell). By contrast, scSLAM-seq requires ~2 million reads to detect ~5,000 genes per cell. Second, scNT-seq is highly scalable, and we successfully analyzed from ~1,000 to >20,000 cells in one experiment. Further, scNT-seq is compatible with cryo-preserved cells, facilitating simultaneous handling of multiple samples. Third, scNT-seq costs <\$0.50 per cell for library preparation and sequencing, which is >50-fold more cost-effective than SMART-seq/plate-based methods.

We note that the standard scNT-seq protocol permits amplification of full-length cDNAs and can be further optimized to capture metabolically labeled, full-length transcript isoforms using a long-read sequencing approach<sup>35</sup> and to uncover temporal information about mRNA processing events. TimeLapse chemistry can also utilize 6-thioguanine to mark new RNAs with G-to-A conversions<sup>36</sup>. Thus, dual labeling of cells with 4sU and 6-thioguanine followed by

**Fig. 5 | Analysis of time-resolved regulon activities and TET-dependent regulation of the stepwise pluripotent-to-2C transition.** **a**, Experimental schematic of identifying time-resolved regulon activity across stem cell states. **b**, Line plots showing the fold changes of new and old RNA abundances of *Tet1* and *Zscan4d* in intermediate and 2C-like states relative to pluripotent states. **c**, Clustered heat maps showing regulon activities inferred from new and old RNA levels across three stem cell states. **d**, UMAP visualization of WT ( $n = 4,633$  cells) and *Tet*-TKO ( $n = 2,319$  cells) mESCs colored by genotypes (left) or stem cell states (right). **e**, Fractions of three stem cell states in two biological replicates (rep1 and rep2) of WT and *Tet*-TKO mESC cultures. **f**, Volcano plots showing genes differentially expressed between WT and *Tet*-TKO mESCs in three stem cell states. Genes significantly upregulated (red) or downregulated (blue) in *Tet*-TKO cells were identified by a two-sided Wilcoxon rank-sum test (Bonferroni-adjusted  $P$  value < 0.05). Both *Tet1* and *Tet2* were significantly decreased in *Tet*-TKO cells. Cell number, WT:  $n = 4,532$  (pluripotent), 47 (intermediate) and 30 (2C-like); *Tet*-TKO:  $n = 2,168$  (pluripotent), 51 (intermediate) and 53 (2C-like). The list of differentially expressed genes and their  $P$  values are shown in Supplementary Table 6. **g**, GO enrichment analysis of genes significantly downregulated or upregulated in *Tet*-TKO mESCs (pluripotent state). ER, endoplasmic reticulum. Significance of enrichment was determined with a hypergeometric test and color scaled by  $-\log_{10}$ (FDR-adjusted  $P$  value).  $P$  values are available as source data.

scNT-seq can enable two independent transcriptomic recordings in single cells, permitting time-series experimental designs to untangle complex RNA regulatory mechanisms and to predict past and

future cell states over an extended time period. High-throughput time-resolved single-cell transcriptomics thus provides a broadly applicable strategy to investigate dynamic biological systems.



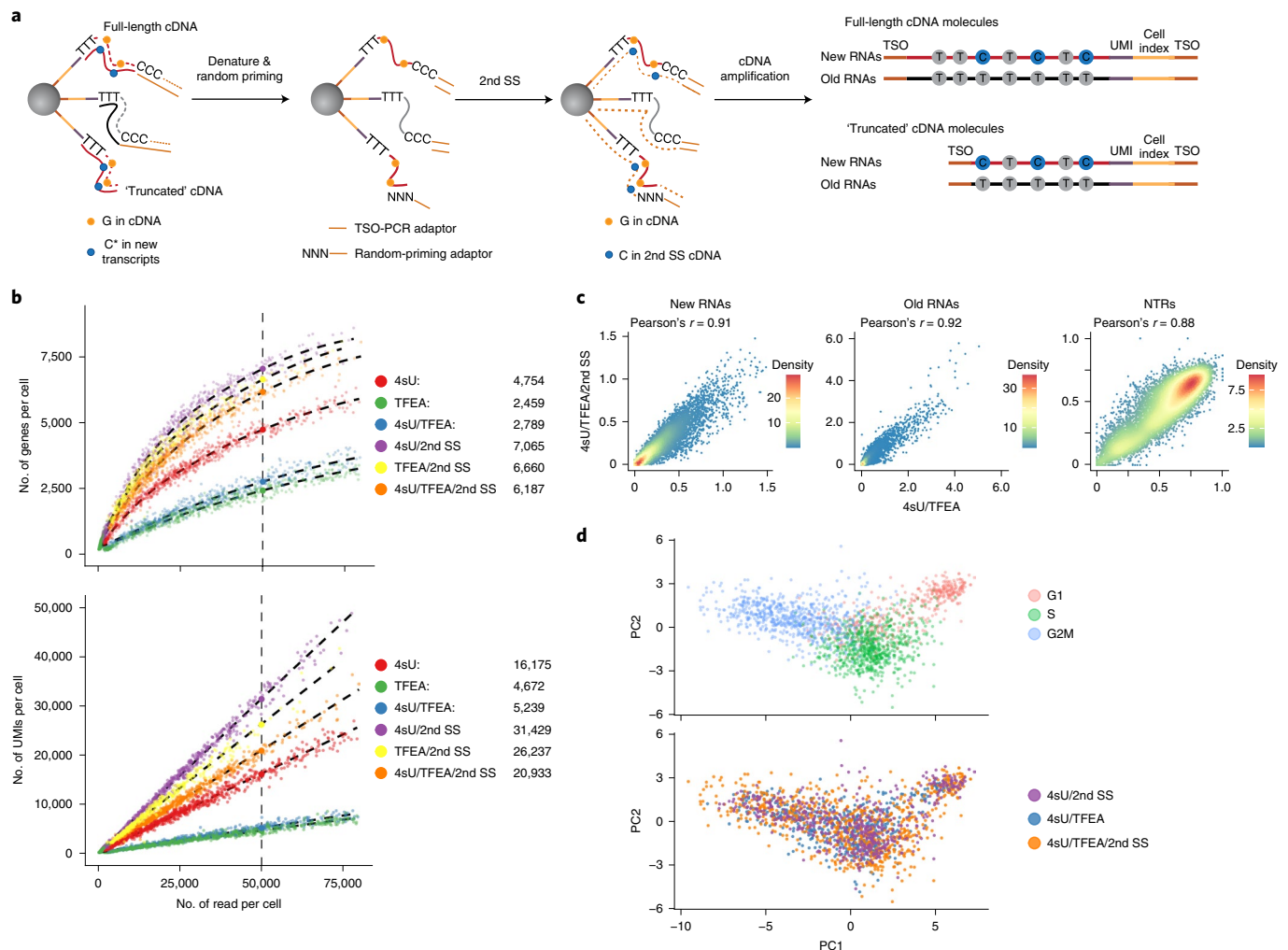


**Fig. 6 | Second-strand synthesis reaction enhances the efficiency of scNT-seq. a**, 2nd SS reaction workflow in scNT-seq. **b**, Scatterplots comparing the number of genes (top) or UMIs (bottom) detected per cell as a function of aligned reads per cell between 4sU ( $n = 692$  cells), TFEA ( $n = 447$ ), 4sU/TFEA ( $n = 533$ ), 4sU/2nd SS ( $n = 515$ ), TFEA/2nd SS ( $n = 400$ ) and 4sU/TFEA/2nd SS ( $n = 795$ ) experiments. 4sU, metabolic labeling with 4sU (100  $\mu$ M; 4 h); TFEA, on-bead TFEA/ $\text{NaIO}_4$  chemical reaction. The fitted lines for each experiment and estimated numbers of genes or UMIs detected per cell at matching sequencing depth (50,000 reads per cell) for different experiments are shown. **c**, Scatterplots showing Pearson's correlation for new and old RNA abundances and NTRs between standard (4sU/TFEA) and 2nd SS (4sU/TFEA/2nd SS) scNT-seq protocols. Levels of new and old RNAs are in natural log transformation of (TP10K + 1). **d**, PCA plots showing K562 cells colored by cell-cycle states (top) or experiments (bottom).

### Online content

Any methods, additional references, Nature Research reporting summaries, source data, extended data, supplementary information, acknowledgements, peer review information; details of author contributions and competing interests; and statements of data and code availability are available at <https://doi.org/10.1038/s41592-020-0935-4>.

Received: 20 December 2019; Accepted: 22 July 2020;  
Published online: 31 August 2020

### References

- Rabani, M. et al. Metabolic labeling of RNA uncovers principles of RNA production and degradation dynamics in mammalian cells. *Nat. Biotechnol.* **29**, 436–442 (2011).
- Rabani, M. et al. High-resolution sequencing and modeling identifies distinct dynamic RNA regulatory strategies. *Cell* **159**, 1698–1710 (2014).
- Tanay, A. & Regev, A. Scaling single-cell genomics from phenomenology to mechanism. *Nature* **541**, 331–338 (2017).
- Herzog, V. A. et al. Thiol-linked alkylation of RNA to assess expression dynamics. *Nat. Methods* **14**, 1198–1204 (2017).
- Schofield, J. A., Duffy, E. E., Kiefer, L., Sullivan, M. C. & Simon, M. D. TimeLapse-seq: adding a temporal dimension to RNA sequencing through nucleoside recoding. *Nat. Methods* **15**, 221–225 (2018).
- Riml, C. et al. Osmium-mediated transformation of 4-thiouridine to cytidine as key to study RNA dynamics by sequencing. *Angew. Chem. Int. Ed. Engl.* **56**, 13479–13483 (2017).
- Erhard, F. et al. scSLAM-seq reveals core features of transcription dynamics in single cells. *Nature* **571**, 419–423 (2019).
- Hendriks, G. J. et al. NASC-seq monitors RNA synthesis in single cells. *Nat. Commun.* **10**, 3138 (2019).
- Macosko, E. Z. et al. Highly parallel genome-wide expression profiling of individual cells using nanoliter droplets. *Cell* **161**, 1202–1214 (2015).
- Hu, P. et al. Dissecting cell-type composition and activity-dependent transcriptional state in mammalian brains by massively parallel single-nucleus RNA-seq. *Mol. Cell* **68**, 1006–1015 (2017).
- Hu, P. et al. Single-nucleus transcriptomic survey of cell diversity and functional maturation in postnatal mammalian hearts. *Genes Dev.* **32**, 1344–1357 (2018).

12. Lake, B. B. et al. Integrative single-cell analysis of transcriptional and epigenetic states in the human adult brain. *Nat. Biotechnol.* **36**, 70–80 (2018).
13. Habib, N. et al. Massively parallel single-nucleus RNA-seq with DroNc-seq. *Nat. Methods* **14**, 955–958 (2017).
14. Qiu, Q. et al. Massively parallel and time-resolved RNA sequencing in single cells with scNT-seq. *Protocol Exchange* <https://doi.org/10.21203/rs.3.pev-1019/v1> (2020).
15. Yap, E. L. & Greenberg, M. E. Activity-regulated transcription: bridging the gap between neural activity and behavior. *Neuron* **100**, 330–348 (2018).
16. Tyssowski, K. M. et al. Different neuronal activity patterns induce different gene expression programs. *Neuron* **98**, 530–546 (2018).
17. Duffy, E. E., Schofield, J. A. & Simon, M. D. Gaining insight into transcriptome-wide RNA population dynamics through the chemistry of 4-thiouridine. *Wiley Interdiscip. Rev. RNA* **10**, e1513 (2019).
18. Aibar, S. et al. SCENIC: single-cell regulatory network inference and clustering. *Nat. Methods* **14**, 1083–1086 (2017).
19. Kannan, M. B., Solovieva, V. & Blank, V. The small MAF transcription factors MAFF, MAFK and MAFK: current knowledge and perspectives. *Biochim. Biophys. Acta* **1823**, 1841–1846 (2012).
20. La Manno, G. et al. RNA velocity of single cells. *Nature* **560**, 494–498 (2018).
21. Schwalb, B. et al. TT-seq maps the human transient transcriptome. *Science* **352**, 1225–1228 (2016).
22. Qiu, X. et al. Mapping vector field of single cells. Preprint at *bioRxiv* <https://doi.org/10.1101/696724> (2019).
23. Kolodziejczyk, A. A. et al. Single cell RNA-sequencing of pluripotent states unlocks modular transcriptional variation. *Cell Stem Cell* **17**, 471–485 (2015).
24. Macfarlan, T. S. et al. Embryonic stem cell potency fluctuates with endogenous retrovirus activity. *Nature* **487**, 57–63 (2012).
25. Eckersley-Maslin, M. A. et al. MERVL/Zscan4 network activation results in transient genome-wide DNA demethylation of mESCs. *Cell Rep.* **17**, 179–192 (2016).
26. Fu, X., Wu, X., Djekidel, M. N. & Zhang, Y. Myc and Dnmt1 impede the pluripotent to totipotent state transition in embryonic stem cells. *Nat. Cell Biol.* **21**, 835–844 (2019).
27. Lu, F., Liu, Y., Jiang, L., Yamaguchi, S. & Zhang, Y. Role of Tet proteins in enhancer activity and telomere elongation. *Genes Dev.* **28**, 2103–2119 (2014).
28. Russo, J., Heck, A. M., Wilusz, J. & Wilusz, C. J. Metabolic labeling and recovery of nascent RNA to accurately quantify mRNA stability. *Methods* **120**, 39–48 (2017).
29. Battich, N. et al. Sequencing metabolically labeled transcripts in single cells reveals mRNA turnover strategies. *Science* **367**, 1151–1156 (2020).
30. Wu, H. & Zhang, Y. Reversing DNA methylation: mechanisms, genomics and biological functions. *Cell* **156**, 45–68 (2014).
31. Wu, H. et al. Dual functions of Tet1 in transcriptional regulation in mouse embryonic stem cells. *Nature* **473**, 389–393 (2011).
32. Wang, H. et al. One-step generation of mice carrying mutations in multiple genes by CRISPR–Cas-mediated genome engineering. *Cell* **153**, 910–918 (2013).
33. Hughes, T. K. et al. Highly efficient, massively-parallel single-cell RNA-seq reveals cellular states and molecular features of human skin pathology. Preprint at *bioRxiv* <https://doi.org/10.1101/689273> (2019).
34. Cao, J., Zhou, W., Steemers, F., Trapnell, C. & Shendure, J. Sci-fate characterizes the dynamics of gene expression in single cells. *Nat. Biotechnol.* <https://doi.org/10.1038/s41587-020-0480-9> (2020).
35. Gupta, I. et al. Single-cell isoform RNA sequencing characterizes isoforms in thousands of cerebellar cells. *Nat. Biotechnol.* <https://doi.org/10.1038/nbt.4259> (2018).
36. Kiefer, L., Schofield, J. A. & Simon, M. D. Expanding the nucleoside recoding toolkit: revealing RNA population dynamics with 6-thioguanosine. *J. Am. Chem. Soc.* **140**, 14567–14570 (2018).

**Publisher's note** Springer Nature remains neutral with regard to jurisdictional claims in published maps and institutional affiliations.

© The Author(s), under exclusive licence to Springer Nature America, Inc. 2020

## Methods

**mESC cultures and metabolic labeling.** WT and *Tet*-TKO J1 mESCs from the American Type Culture Collection (ATCC, SCRC-1010) were cultured in the presence of Mitomycin C-inactivated mouse embryonic fibroblasts on 0.1% gelatin-coated (Millipore, ES-006-B) six-well plates in DMEM (Gibco, 11965084) supplemented with 15% fetal bovine serum (Gibco, 16000044), 0.1 mM nonessential amino acid (Gibco, 11140050), 1 mM sodium pyruvate (Gibco, 11360070), 2 mM L-glutamine (Gibco, 25030081), 50  $\mu$ M 2-mercaptoethanol (Gibco, 31350010), 1  $\mu$ M MEK inhibitor PD0325901 (Axon Med Chem, Axon 2128), 3  $\mu$ M GSK3 inhibitor CHIR99021 (Axon Med Chem, Axon 2128) and 1,000 U ml<sup>-1</sup> leukemia inhibitory factor (Gemini Bio-Products, 400-495-7). Cells were maintained at 37°C with 5% CO<sub>2</sub> and passaged every 2–3 d. The average doubling time of J1 mESCs in the presence of 4sU as determined by cell counting was 14.8 h.

For labeling experiments, 4sU (Alfa Aesar, J60679) was dissolved in dimethylsulfoxide to make 1 M stock. WT and *Tet*-TKO mESCs were seeded at a density of  $3 \times 10^5$  cells per ml 2 d before the labeling experiments and cultured in feeder-free conditions (0.1% gelatin-coated plates). One time-point 4sU labeling was performed by incubating mESCs in fresh medium supplemented with 4sU (at a final concentration of 100  $\mu$ M). After 4 h of labeling, mESCs were rinsed once with PBS and dissociated into single-cell suspensions with TrypLE-Express (Gibco, 12605010) for 5 min at 37°C.

**CRISPR–Cas9 genome editing in mESCs.** *Tet*-TKO J1 mESCs were generated by CRISPR–Cas9 genome editing using previously validated guide RNAs (gRNAs)<sup>32</sup>. Briefly, gRNA oligonucleotides were cloned into lentiCRISPR v2 vector (Addgene 52961) as described<sup>37</sup>. After reaching ~70% confluency on 0.1% gelatin-coated six-well plates, WT J1 mESCs were dissociated and 2 million cells were co-transfected with 1  $\mu$ g of lentiCRISPRv2-sgTet1, 1  $\mu$ g of lentiCRISPRv2-sgTet2 and 1  $\mu$ g of lentiCRISPRv2-sgTet3 vectors in suspension using Lipofectamine 2000 (Invitrogen, 11668019) as recommended by the manufacturer. Three days after transfection, 30,000 transfected mESCs were seeded on a 10-cm dish coated with 0.1% gelatin in the presence of mitotically inactivated feeder cells, and 0.5  $\mu$ g ml<sup>-1</sup> puromycin was added to enrich transfected mESCs for 2 d. After 14 d, single colonies were picked and expanded in 24-well plates. DNA isolation, PCR amplification of *Tet1*, *Tet2* and *Tet3* loci and Sanger sequencing was performed to genotype the clonal cell lines. Inactivation of *Tet1–3* was further confirmed by the lack of 5-hydroxymethylcytosine via mass spectrometry as described<sup>38</sup>.

**Human K562 cell cultures and species-mixing experiments.** Human K562 cells (ATCC, CCL-243) were maintained at 37°C with 5% CO<sub>2</sub> in RPMI medium supplemented with 10% fetal bovine serum (Sigma, F6178) in a T75 flask and passaged every 3 d. For species-mixing experiments, the mESCs or K562 cells were seeded at  $3 \times 10^5$  cells per ml the day before the experiment and incubated with medium supplemented with 100  $\mu$ M 4sU. After 4 h of labeling, mESCs and K562 cells were washed once with PBS and harvested for scNT-seq analysis.

**Mouse cortical neuronal culture and activity stimulation.** Mouse cortices were dissected from embryonic day 16 (E16) C57BL/6 embryos of mixed sex (Charles River). Cortical neurons were dissociated with papain (Worthington) and plated on six-well plates (at a density of ~600,000 cells per well) coated with poly-L-ornithine (30 mg ml<sup>-1</sup>; Sigma, P2533). Mouse cortical neuronal cultures were maintained in neurobasal medium (Gibco, 21103049) supplemented with B27 (Gibco, 17504044), 2 mM GlutaMAX (Gibco, 35050061), and 1 $\times$  penicillin–streptomycin (Gibco, 15140122). Mouse experiments were conducted in accordance with the ethical guidelines of the National Institutes of Health and with the approval of the Institutional Animal Care and Use Committee of the University of Pennsylvania.

After 4 d of in vitro culture, primary cortical cultures were stimulated with a final concentration of 55 mM KCl for various durations (0, 15, 30, 60 and 120 min). For metabolic labeling, neuronal cultures were incubated with medium supplemented with 200  $\mu$ M 4sU. After 2 h of labeling, cells were washed once with PBS, digested in 0.05% trypsin-EDTA (Gibco, 25300054) for 20 min at 37°C and harvested in PBS with a cell scraper.

**Cell fixation, cryopreservation and rehydration for sample processing.** Cultured mESCs in six-well plates were digested with TrypLE-Express and harvested as aforementioned. The cells were washed once with PBS and were resuspended with 0.4 ml of PBS containing 0.01% BSA. Cells were split into two 1.5 ml LoBind tubes (Eppendorf) and 0.8 ml of methanol was added dropwise, yielding a final concentration of 80% methanol in PBS. After mixing and incubating the cell suspension on ice for 1 h, the methanol-fixed cells were then stored at –80°C for up to 1 month. For sample rehydration, cells were removed from –80°C and kept on ice throughout the procedure. After cells were spun down at 1,000g for 5 min at 4°C, methanol-PBS solution was removed, and cells were resuspended in 1 ml of rehydration buffer. After cell counting, the single-cell suspension was diluted to 100 cells per  $\mu$ l and immediately used for scNT-seq analysis. We compared two rehydration buffers (PBS based<sup>39</sup>: 0.01% BSA in PBS supplemented with 0.5% RNase inhibitor (Lucigen, 30281-2); SSC based<sup>40</sup>: 3 $\times$  SSC, 40 mM dithiothreitol (DTT), 0.04% BSA and 1% RNase inhibitor; Extended Data Fig. 1c) and observed similar performance.

**Pulse-chase experiment for RNA half-life analysis.** mESCs were seeded at a density of  $3 \times 10^5$  cells per ml the day before the experiment. 4sU metabolic labeling was performed by incubating mESCs in fresh medium supplemented with 200  $\mu$ M 4sU, and media were exchanged every 4 h for the duration of the 24-h pulse. For the uridine chase experiment, cells were washed twice with PBS and incubated with fresh medium supplemented with 10 mM uridine (Sigma, U6381). At the respective time points (0, 0.5, 1, 3, 6, 12 and 24 h), cells were harvested, methanol fixed as aforementioned and stored at –80°C for later use. On the day of performing droplet microfluidics assays, all samples were rehydrated (PBS-based buffer) and analyzed in parallel. Clustering analysis based on total RNAs separated mESCs (combined from seven time points) into three stem cell states (pluripotent, 97.4%  $\pm$  0.78%; intermediate, 1.5%  $\pm$  0.49%; and 2C-like, 1.1%  $\pm$  0.38%), suggesting that our pulse-chase experiments did not substantially alter the state transition.

**scNT-seq library preparation and sequencing.** A step-by-step protocol of scNT-seq is provided as a Supplementary Protocol and is also available at Protocol Exchange<sup>14</sup>. Droplet microfluidics-based cell and barcoded bead co-encapsulation, library preparation and sequencing were performed as previously described with minor modifications<sup>10,11</sup>. Specifically, the single-cell suspension was counted (Countess II system) and diluted to a concentration of 100 cells per  $\mu$ l in PBS containing 0.01% BSA. The flow rates for cells and beads were set to 3.200  $\mu$ l per hour, while QX200 droplet generation oil (Bio-rad) was run at 12,500  $\mu$ l per hour.

Next, droplets were broken by adding perfluoro-1-octanol (Sigma-Aldrich). After droplet breakage, the beads were treated with TimeLapse chemistry to convert 4sU to a cytidine analog<sup>3</sup>. Briefly, 50,000–100,000 beads were washed once with 450  $\mu$ l of washing buffer (1 mM EDTA, and 100 mM sodium acetate (pH 5.2)), then the beads were resuspended with a mixture of TFEA (600 mM), EDTA (1 mM) and sodium acetate (pH 5.2; 100 mM) in water. NaIO<sub>4</sub> was then added to the reaction at a final concentration of 10 mM and incubated at 45°C for 1 h with rotation. The beads were washed once with 1 ml TE buffer, then incubated in 0.5 ml 1 $\times$  reducing buffer (10 mM DTT, 100 mM NaCl, 10 mM Tris (pH 7.4) and 1 mM EDTA) at 37°C for 30 min with rotation, followed by washing once with 0.3 ml 2 $\times$  reverse transcription buffer.

After one-pot chemical conversion reaction on pooled beads, the remaining library preparation steps were performed as previously described<sup>3</sup>. Specifically, for up to 120,000 beads, 200  $\mu$ l of reverse transcription mix (1 $\times$  Maxima reverse transcription buffer (Thermo Fisher), 4% Ficoll PM-400, 1 mM dNTPs (Clontech), 1 U per  $\mu$ l RNase inhibitor, 2.5  $\mu$ M template switch oligo (TSO: AAGCAGTGGTATCAACGCAGAGTGAATrGrGrG) and 10 U per  $\mu$ l Maxima H Minus reverse transcriptase (Thermo Fisher)) were added. The reverse transcription reaction was incubated at room temperature for 30 min, followed by incubation at 42°C for 120 min. After Exonuclease I treatment and determining the optimal number of PCR cycles for cDNA amplification as previously described<sup>10</sup>, we prepared PCR reactions (~6,000 beads per tube) for all barcoded beads collected for each scNT-seq run in a volume of 50  $\mu$ l (25  $\mu$ l of 2 $\times$  KAPA HiFi hotstart readymix (KAPA biosystems), 0.4  $\mu$ l of 100  $\mu$ M TSO-PCR primer (AAGCAGTGGTATCAACGCAGAGT)<sup>10</sup> and 24.6  $\mu$ l of nuclease-free water) and amplified full-length cDNA with the following thermal cycling parameter (95°C for 3 min; 4 cycles of (98°C for 20 s, 65°C for 45 s and 72°C for 3 min); 9–12 cycles of (98°C for 20 s, 67°C for 45 s and 72°C for 3 min); 72°C for 5 min and hold at 4°C). We then tagged cDNA using the Nextera XT DNA sample preparation kit (Illumina, FC-131-1096), starting with 550–1,000 pg of cDNA pooled from all PCR reactions of a sample. After cDNA tagging, we further amplified the library with 12 enrichment cycles using the Illumina Nextera XT i7 primers along with the P5-TSO hybrid primer (AATGATACGGCACCACCGATC TACACGCCTGTCCGCGGAAGCAGTGGTATCAACGCAGAGT\*<sup>3</sup>A\*C). After quality-control analysis using a Bioanalyzer (Agilent), libraries were sequenced on an Illumina NextSeq 500 instrument with the 75- or 150-cycle High Output v2 or v2.5 kit (Illumina). We loaded the library at 2.0 pM and added Custom Read1 Primer (GCCTGTCCGCGGAAGCAGTGGTATCAACGCAGAGTAC) at 0.3  $\mu$ M to position 7 of the reagent cartridge. Paired-end sequencing was performed on an Illumina NextSeq 500 sequencer as described previously<sup>11</sup>. The sequencing configuration was 20 bp (Read 1), 8 bp (Index 1) and 60 or 130 bp (Read 2).

**SLAM-seq reaction on barcoded beads.** After droplet breakage, the beads were washed once with NaPO<sub>4</sub> buffer with 30% dimethylsulfoxide (50 mM, pH 8.0) and then incubated in 500  $\mu$ l of reaction mixture containing 10 mM IAA for either 15 min at 50°C (standard condition) or 1 h at 45°C (modified condition)<sup>4</sup>. The reaction was stopped by adding 10  $\mu$ l of 1 M DTT to a final concentration of 20 mM. Note that the library for Fig. 1b (IAA reaction) was generated with the modified condition because we could not efficiently amplify cDNA using the standard reaction condition.

**Second-strand synthesis on barcoded beads.** After exonuclease I treatment, pooled beads were washed once with TE-SDS buffer and twice with TE-TW buffer. The beads were resuspended in 500  $\mu$ l of 0.1 M NaOH and incubated for 5 min at room temperature with rotation, and 500  $\mu$ l of 0.2 M Tris-HCl (pH 7.5) was then added to neutralize the solution. The beads were washed once with TE-TW buffer and once with 10 mM Tris-HCl (pH 8.0). For the 2nd SS reaction, the beads

were resuspended in 200  $\mu$ l of reaction mixture (1 $\times$  Blue buffer (Enzymatics), 4% Ficoll PM-400, 1 mM dNTPs (Clontech), 2.5  $\mu$ M Template Switch Oligo-GAATG (TSO-GAATG: /5SpC3/AAGCAGTGGTATCAACGCAGAGTGAATG), 5  $\mu$ M TSO-N9 (TSO-N9: /5SpC3/AAGCAGTGGTATCAACGCAGAGTGAAT (N1:25252525)(N1)(N1)(N1)(N1)(N1)(N1)(N1)(N1)(N1)(N1)), N1 represents a mixture of A, T, C and G at a 25:25:25:25 ratio) and 1.25 U  $\mu$ l<sup>-1</sup> Klenow exo- (Enzymatics)). The reaction was incubated at room temperature for 10 min, followed by incubation at 37 °C for 1 h with rotation. The reaction was stopped by washing the beads once with TE-SDS buffer and twice with TE-TW buffer.

#### Read alignment and quantification of metabolically labeled transcripts.

Paired-end sequencing reads of scNT-seq were processed as previously described<sup>10</sup> with some modifications. Each mRNA read (Read 2) was tagged with the cell barcode (bases 1–12 of Read 1) and UMI (bases 13–20 of Read 1), trimmed of sequencing adaptors and poly-A sequences, and aligned to the mouse (mm10, Gencode release vM13), human (GRCh38, Gencode release v23) or a concatenated mouse and human (for the species-mixing experiment) reference genome assembly using STAR v2.5.2a. Both exonic and intronic reads that mapped to predicted strands of annotated genes were retained for the downstream analysis. To quantify the labeled and unlabeled transcripts, uniquely mapped reads with a mapping score of >10 were grouped by UMI indices in every cell and were used to determine the T-to-C substitution using sam2tsv (<https://github.com/lindenb/jvarkit>; version ec2c2364). T-to-C substitutions with a base Phred quality score of >27 were retained. For each experiment, sites with background T-to-C substitutions (present in the control sample without TFEA/NaIO<sub>3</sub> treatment) were determined and excluded for T-to-C substitution identification. After correcting background mutations, a UMI/transcript was defined as labeled if there was at least one T-to-C substitution in any one of the reads linked to the same UMI index. Every UMI could then be assigned as labeled or unlabeled based on presence of T-to-C substitutions (Fig. 1d). For each transcript, the total number of uniquely labeled and unlabeled UMI sequences were counted and, finally, were assembled into matrices using the gene name as rows and cell barcode as columns. Thus, each cell was associated with two digital gene expression matrices (labeled or unlabeled transcripts) from the scNT-seq sequencing data.

**Cell-type clustering and dataset integration.** The raw digital expression matrices of new and old UMI counts were summed up and loaded into the R package Seurat. For normalization, UMI counts for all cells were scaled by library size (total UMI counts), multiplied by 10,000 and transformed to log space. Only genes detected in >10 cells were retained. Cells with a relatively high percentage of UMIs mapped to mitochondrial genes ( $\geq 5\%$ ) were discarded. Cells with fewer than 500 or more than 5,000 detected genes were also removed.

For mouse cortical neurons (Fig. 2a), we used Seurat (v2.3.4)<sup>41</sup> for downstream analysis. After removing low quality cells, 20,547 mouse cortical cells were retained. HVGs were identified using the function FindVariableGenes in Seurat with the parameters  $x.low.cutoff = 0.05$  and  $y.cutoff = 0.5$ , resulting in 2,290 HVGs. The expression level of HVGs in the cells was scaled and centered for each gene across cells and was subjected to PCA. The most significant 30 PCs were selected and used for two-dimension reduction by UMAP<sup>42</sup> in Seurat with the default parameters. Clusters were identified using the function FindCluster in Seurat with the resolution parameter set to 1. To identify major cell types, we merged adjacent clusters in UMAP that showed high expression levels of excitatory neuronal markers (*Neurod2* and *Neurod6*) and defined it as the ‘Ex’ cluster.

For the RNA-decay experiment (Fig. 4b), 20,190 cells were kept for downstream analysis after quality filtering. Seurat 3 (v3.1.4)<sup>43</sup> was used to align cells from different time points. The top 2,000 HVGs were identified using the function FindVariableFeatures with the vst method. Canonical correlation analysis (CCA) was used to identify common sources of variation among different time points. The first 30 dimensions of the CCA were chosen for integration. The expression levels of HVGs were then scaled and centered for each gene across cells, and PCA was performed on the scaled data. The 20 most significant PCs were selected and used for two-dimension reduction by UMAP. Clusters were identified using the function FindCluster in Seurat with the resolution parameter set to 2. After UMAP projection, a small cell cluster ( $n = 131$  cells, 0.65% of input cells) was identified as ‘partially differentiated mESCs’ based on previously identified markers (*Cryab*, *S100a6*, *Thbs1*, *Krt7*, *Gsn*, *Krt19* and *Krt8*)<sup>23</sup> and was thus excluded. Adjacent clusters with high levels of *Sox2* were combined to a single ‘pluripotent’ state cluster. Thus, 20,059 cells were assigned to three principal stem cell states (pluripotent, intermediate and 2C-like). Cell-type-specific markers were identified using the function FindMarkers in Seurat with a two-sided Wilcoxon rank-sum test with default parameters.

To enable directly comparative analyses within cell states between WT and *Tet*-TKO mESCs (Fig. 5d), we used Seurat 3 (v3.0.0.9000) to perform joint analysis. After quality filtering, 4,633 WT cells and 2,319 *Tet*-TKO cells were retained. The top 2,000 HVGs were identified using the function FindVariableFeatures with the vst method. CCA was used to identify common sources of variation between WT and *Tet*-TKO cells. The first 20 dimensions of the CCA were chosen to integrate the two datasets. After integration, the expression level of HVGs in the cells was scaled and centered for each gene across cells, and PCA analysis was performed

on the scaled data. The 20 most significant PCs were selected and used for two-dimension reduction by UMAP. Clusters were identified using the function FindCluster in Seurat with the resolution parameter set to 3. As aforementioned, adjacent clusters with high expression levels of *Sox2* were combined to a single pluripotent cluster.

**Estimation of the fraction of newly synthesized transcripts.** Current metabolic labeling strategy typically results in incomplete 4sU labeling of all newly transcribed RNAs in single cells<sup>7,8</sup>. To overcome this issue, we adapted a binomial mixture model-based statistical correction strategy<sup>5,44</sup> and optimized it for UMI-based scNT-seq datasets. For each experiment, the data were modeled as the mixture of two binomial distributions to approximate the number of T-to-C substitutions  $y_i$  for each gene transcript  $i$ , with its likelihood function as

$$f(\theta, p, q) = \theta \text{Binom}(y_i; p, n_i) + (1 - \theta) \text{Binom}(y_i; q, n_i)$$

where  $\theta$  is the fraction of new transcripts in each experiment,  $p$  and  $q$  are the probabilities of a T-to-C substitution at each nucleotide for new and old transcripts, respectively, and  $n_i$  is the number of uridine nucleotides observed in the transcript  $i$ . A consensus sequence for each transcript is built by pooling reads with the same UMI index and taking the most frequent variant at each position. 10,000 UMIs were randomly sampled and the global substitution probabilities  $p$  and  $q$  were estimated based on the above mixture model. The model was fit by maximizing the likelihood function using the Nelder–Mead algorithm. The optimization was repeated ten times with random initialization values for  $\theta$ ,  $p$ , and  $q$  in the range [0,1], keeping the best fit with  $\theta \in [0,1]$ .

To obtain enough UMIs for global parameters estimation at each time point of mouse cortical neuronal culture datasets, four inhibitory neuronal clusters (Inh 2–4 and Inh-NP) were combined based on transcriptomic similarity, and three non-neuronal clusters (Ex-NP1, Ex-NP2 and RG) were also aggregated. Thus, four major cell clusters (Ex, Inh1 and two combined clusters) were subjected to statistical modeling separately. For mESC datasets, we assumed that *Tet*-TKO would not affect 4sU incorporation rate and thus combined WT and *Tet*-TKO datasets to estimate unified global parameters,  $p$  and  $q$ , for three stem cell states (pluripotent, intermediate and 2C-like). In sum, 20 sets of  $p$  and  $q$  (5 time points  $\times$  4 combined clusters) were determined in cortical neuronal datasets and 3 sets of  $p$  and  $q$  (pluripotent, intermediate and 2C-like clusters) were estimated for mESC datasets. These global parameters were then used to estimate the fraction of new transcripts.

**Computing aggregated new transcripts for each cell type or state.** For Fig. 2c and Extended Data Fig. 3d, we aggregate all the UMIs belonging to the same cell type and estimated the fraction of new transcripts  $\theta$  for each gene with >100 UMIs in that cell type at each time point. The likelihood function for the mixture model above was maximized using the Brent algorithm with the constraint  $\theta \in [10^{-8}, 1]$ . The 95% confidence interval was calculated from the Hessian matrix, and  $\theta$  estimates for genes with a confidence interval greater than 0.2 were removed. The level of new transcript ( $N$ ) was then estimated:

$$N = \theta(L + U)$$

where  $\theta$  is the fraction of newly transcribed RNAs for a gene in a cell type,  $L$  is the number of labeled transcripts of a gene and  $U$  is the number of unlabeled transcripts of a gene. The level of old transcript was calculated by  $(1 - \theta)(L + U)$ .

**Computing new transcripts in single cells.** While the fraction of new transcripts could theoretically be estimated for each gene in single cells using the aforementioned statistical correction model, due to limited sequencing coverage for single-cell transcriptomes, modeling every gene for tens of thousands of cells was not experimentally feasible and computationally inefficient. We noticed that most genes exhibited a highly similar detection rate,  $\alpha$  (the ratio between observed and corrected new RNA levels), in aggregated scNT-seq datasets (Extended Data Fig. 3d). Under the assumption that 4sU labeling of new transcripts in each cell is largely a stochastic process and may vary between cells, the global metabolic labeling rate in each cell can also provide a good approximation as a binomial process; therefore, the mean detection rate  $\alpha$  of all genes can be estimated for each cell using the same aforementioned statistical model. The single-cell level detection rate  $\alpha$  can be computed by dividing all the labeled transcripts of a cell by the statistically estimated new transcripts of that cell. After removing cells with out-of-range values ( $\alpha > 1$ ), we successfully computed the detection rate  $\alpha$  for 88.3% (18,133 of 20,547) of mouse cortical cells and 95.1% (6,609 of 6,952) of mESCs. The mean detection rates were 60% and 66% in cortical cells and mESCs, respectively. For each gene, the new RNA level was computed as

$$N = \min\left(\frac{L}{\alpha}, (L + U)\right)$$

where  $\alpha$  is the new RNA detection rate of a cell,  $L$  is the number of labeled transcripts of a gene in that cell and  $U$  is the number of unlabeled transcripts of a gene. The number of pre-existing transcripts was calculated by  $L + U - N$ .

The computed new and old transcripts were used for all downstream single-cell analyses, including SCENIC-based single-cell regulon/GRN activity analysis (Figs. 2d,e and 5c) and RNA velocity analysis (Fig. 3 and Extended Data Figs. 4–6).

**GO enrichment analysis.** To identify functional categories associated with defined gene lists, GO annotations were downloaded from the Ensembl database. An enrichment analysis was performed via a hypergeometric test. The  $P$  value was calculated using the following formula:

$$P = 1 - \sum_{i=0}^{m-1} \binom{M}{i} \binom{N-M}{n-i} / \binom{N}{n}$$

where  $N$  is the total number of background genes,  $n$  is the total number of selected genes,  $M$  is the number of genes annotated to a certain GO term and  $i$  is the number of selected genes annotated to a certain GO term.  $P$  values were corrected using the function `p.adjust` with FDR correction in R. GO terms with  $FDR < 0.05$  were considered enriched. All statistical calculations were performed in R.

For enrichment analysis of stable/unstable mRNAs (Extended Data Fig. 8b), genes were ranked by the RNA half-life. The top 10% of genes with the longest half-lives were defined as stable genes, whereas the bottom 10% of genes with the shortest half-lives were considered as unstable. Then, the stable and unstable gene sets were subjected to GO enrichment analysis. For Extended Data Fig. 9b, genes showing >1.5-fold change between pluripotent and 2C-like states were selected and subjected to GO enrichment analysis. For Fig. 5g, significantly differentially expressed genes between WT and *Tet*-TKO mESCs (adjusted  $P$  value < 0.05) were subjected to GO enrichment analysis.

**Identification of differentially expressed genes.** Differential gene expression analysis of new transcripts between different time points of neuronal activation (15, 30, 60 and 120 min) and control (0 min) was performed with the `FindMarkers` function in Seurat using a two-sided Wilcoxon rank-sum test. New transcripts with a fold change > 1.5 and an adjusted  $P$  value < 0.05 (Bonferroni corrected) were considered to be differentially expressed. Neuronal activity-induced genes were further identified if a new transcript was significantly increased in at least one time point with KCl stimulation in at least one cell type (Extended Data Fig. 2d). For MA-plots in Extended Data Fig. 9a, genes showing a >1.5-fold change of new or old RNA expression between pluripotent and 2C-like states were considered differentially expressed. For comparison between WT and *Tet*-TKO mESCs among three stem cell states (Fig. 5f), two-sided Wilcoxon rank-sum test was used to assess significance of the difference, and the  $P$  value was adjusted by Bonferroni correction. Genes with an adjusted  $P$  value < 0.05 were considered as differentially expressed.

**Estimation of RNA half-life.** For each gene, we separately aggregated labeled and unlabeled UMI counts in each cell state (Fig. 4 and Extended Data Fig. 8). Then, the fraction of labeled transcripts was calculated with summed labeled UMI counts divided by total UMI counts (labeled and unlabeled). The fractions of labeled transcripts were corrected for doubling time (14.8 h) and normalized to 0 h of chase. The R function `nl` was used to perform curve fitting with the parameters set to `'y ~ I(a*exp(-b*x))'`, `'start = list(a = 1, b = 0)'` and `'na.action = na.exclude'`. We kept the goodness of fit as  $R^2 > 0.4$ . After filtering out genes expressed in <5% of cells, we determined the RNA half-lives of 1,926 genes that are also commonly detected in bulk SLAM-seq assays<sup>4</sup>.

**Splicing kinetics-based RNA velocity analysis.** For standard RNA velocity analysis (splicing RNA velocity), we first generated the bam files using the Drop-seq analysis pipeline (v1.1.2). The reads were demultiplexed using `dropEst`<sup>45</sup> (v0.8.5) pipeline, with `'-m -V -b -f -L eiEIBA'` to annotate bam files. The genome annotations (mm10; Gencode release vM13) were used to count spliced and unspliced molecules for each experiment. `Dynamo`<sup>22</sup> (<https://github.com/aristoteleo/dynamo-release/>; commit: 9871d78) was then used for RNA velocity analysis. To specifically reveal the neuronal activity-dependent RNA dynamics, we provided `dynamo` with the unspliced and spliced counts of 97 neuronal activity genes as features (Extended Data Fig. 2d and Supplementary Table 2) for PCA denoising, followed by UMAP projection. The estimation assumption and model were set to 'steady states' and 'stochastic', respectively. The high-dimensional velocity vectors were projected to two-dimensional UMAP space and visualized with the streamline plot using `dynamo` with default parameters. Similarly, phase diagrams and randomized streamline plots of velocity vectors were generated using `dynamo` with default settings (Fig. 3a and Extended Data Figs. 4 and 5).

**Metabolic labeling-based RNA velocity analysis.** The original RNA velocity described by La Manno et al.<sup>20</sup> is defined as the rate of changes in spliced mRNAs over time or  $\frac{ds}{dt} = \dot{s} = \beta u - \gamma s$  ( $s$  and  $u$  are the abundance of spliced and unspliced mRNAs in a single cell measured by scRNA-seq, respectively;  $\beta$  and  $\gamma$  are RNA splicing or degradation rates, respectively, while  $t$  is the time). To estimate splicing-based RNA velocity, La Manno et al. assumed a constant splicing rate  $\beta = 1$  that enabled the identifiability of  $\gamma$  when cells are at steady states (when the RNA velocity is 0); that is:

$$\dot{s} = 0 = \beta u - \gamma s, \text{ where } \beta = 1.$$

At steady states,  $u = \gamma s$  and  $\gamma$  can be estimated by linear regression of the expression of spliced and unspliced transcripts  $s$  and  $u$  for each gene. For simplicity, La Manno et al. regarded cells with extreme expressions (that is, the top or bottom five percentiles of all gene expression) as steady-state cells. In the scSLAM-seq study<sup>7</sup>, the authors replaced unspliced and spliced counts with new and total RNA to compute a new form of RNA velocity that they denoted as NTR velocity. However, as discussed below, NTR velocity analysis is only valid under specific metabolic labeling conditions.

To compute a metabolic labeling-based RNA velocity that is generally applicable, we used `dynamo`, which explicitly models metabolic labeling of newly synthesized transcripts. We denoted  $n$  and  $r$  as the new (metabolic labelled RNAs) and total RNA abundance for each gene in each cell, respectively. The velocity of new and total RNA can then be

$$\dot{n} = \alpha - \gamma n,$$

$$\dot{\gamma} = \alpha - \gamma r.$$

Here,  $\alpha$  is the transcription rate (or RNA synthesis rate), while  $\gamma$  is the degradation rate. By solving the differential equation related to new RNA velocity, we have

$$n = \frac{\alpha}{\gamma} (1 - e^{-\gamma t}).$$

After some arrangement, the transcription rate can be further written as

$$\alpha = \frac{n\gamma}{1 - e^{-\gamma t}} \approx \frac{n}{t}.$$

The above approximation is derived from the fact that, by Taylor expansion,  $e^{-\gamma t} \approx 1 - \gamma t$ . Thus, the velocity for the total RNA is

$$\dot{r} = \frac{n}{t} - \gamma r.$$

If we replace new RNA as the unspliced RNA, and total RNA as the spliced RNA as described for NTR velocity, we have

$$\dot{s} = \frac{u}{t} - \gamma s.$$

Interestingly, if  $t$  is around 1 h (which is the case for scSLAM-seq<sup>7</sup> and our study), we can have  $\dot{s} = u - \gamma s$ , the same equation used by the original RNA velocity. Thus, the NTR velocity is an approximation of the total RNA velocity.

In the `dynamo` model<sup>22</sup>, the NTR velocity is extended so that it is not conditioned on that  $t \approx 1$ , using the same steady-state assumption. At the steady states, denoting the slope of the regression line of the NTR velocity as  $k$ , we have

$$r_{ss} = \frac{\alpha}{\gamma},$$

$$n = k r_{ss}.$$

Thus, we have  $n = \frac{\alpha}{\gamma} (1 - e^{-\gamma t}) = r_{ss} (1 - e^{-\gamma t})$ , which leads to  $k = (1 - e^{-\gamma t})$ . Therefore, we can calculate  $\gamma$  and  $\alpha$  as

$$\gamma = \frac{-\ln(1 - k)}{t},$$

$$\alpha = \frac{\gamma n}{k}.$$

We used the above the equations to calculate the 'time-resolved `dynamo` RNA velocity'  $\dot{\gamma}$ :

$$\dot{\gamma} = \frac{-\ln(1 - k)}{kt} n + \frac{\ln(1 - k)}{t} \gamma \Rightarrow \frac{-kt}{\ln(1 - k)} \dot{\gamma} = n - kr.$$

The above result implies that the time-resolved `dynamo` RNA velocity for each gene scales to the NTR velocity via a gene-specific factor  $\frac{-kt}{\ln(1 - k)}$ . This suggests that even when  $t \neq 1$ , the NTR velocity is still informative if  $k$  does not substantially differ across genes. However, NTR velocity lacks physical meaning of how many molecules change per unit time. In our time-resolved `dynamo` RNA velocity implementation, the thickness of directional streamlines in the locally averaged vector field indicates RNA velocity rate (molecules per unit time). Specifically, the new and total RNA counts are provided as input to `dynamo`, and the labeling time is also explicitly supplied for calculating metabolic labeling-based time-resolved RNA velocity (Fig. 3a and Extended Data Figs. 4 and 5). For Fig. 3a and Extended Data Fig. 4a, permutation of velocity flows was performed by shuffling the velocity for genes in each cell and then randomly flipping the sign of shuffled velocity values.

**Estimation of RNA biogenesis rate and degradation rate constant.** The degradation rate constant ( $\gamma$ , units/h) can be calculated from RNA half-life ( $t_{1/2}$ ) using

$$\gamma = \frac{\ln(2)}{t_{1/2}}$$

Then, we assumed the gene-specific RNA biogenesis rate ( $\alpha$ , molecules/h) is a constant for all cells from each cell state, which can then be calculated using

$$\alpha = \frac{n\gamma}{1 - e^{-\gamma t}}$$

where  $n$  is the average labeled RNA abundance for each gene in each state (pluripotent, intermediate or 2C-like),  $\gamma$  is the degradation rate constant in each state and  $t$  (units in h) is the metabolic labeling time.

To define gene-specific RNA regulatory strategies for the transition from pluripotent to intermediate and 2C-like states in mESCs (Fig. 4e), we computed the Pearson correlation coefficient  $r$  between the degradation rate and transcription rate constant. To determine the RNA regulatory strategy as previously described<sup>29</sup>, we defined genes with a strong negative Pearson correlation coefficient ( $r \leq -0.5$ ) as a cooperative strategy, a strong positive Pearson correlation coefficient ( $r \geq 0.5$ ) as a destabilizing strategy and a moderate Pearson correlation coefficient ( $-0.5 < r < 0.5$ ) as a neutral strategy.

**Analysis of single-cell regulon activity using new and old RNAs.** To assess the regulatory activity of TFs associated with different cell states or cell types, we used SCENIC<sup>18</sup> (v1.1.2.2) to perform single-cell GRN or regulon activity analysis. Regulatory modules are identified by inferring coexpression between TFs and genes containing a TF-binding motif in their promoters. We first separated the expression matrix into two parts based on the expression level of new and old transcripts, then provided them as inputs to SCENIC analysis, which enabled us to identify specific regulatory modules associated with either new or old transcriptomes from the same cell. Two gene-motif rankings, 10 kb around the transcription start site and 500 bp upstream, were loaded from RcisTarget databases (mmm9). Genes detected in >1% of all cells and listed in the gene-motif ranking databases were retained. To this end, 8,744 genes in mouse cortical neuronal culture datasets and 9,388 genes in mESC datasets were subjected to downstream analysis. Then, GRNBoost (implemented in pySCENIC) was used to infer the coexpression modules and to quantify the weight between TFs and target genes. Targets genes that did not show a positive correlation (>0.03) in each TF module were discarded. SCENIC identified 4,944 and 5,406 TF modules in mouse cortical neuronal culture and mESC datasets, respectively. The *cis*-regulatory motif analysis on each of the TF modules using RcisTarget revealed 277 and 325 regulons in cortical culture and mESC datasets, respectively. The top 1% of the number of detected genes per cell was used to calculate the enrichment of each regulon in each cell. For Figs. 2d and 5c, we computed the mean area under the curve (AUC) of all cells belonging to defined groups, and then scaled the mean AUC using the scale function in R. The R package pheatmap was used to generate the heat map. For Fig. 3d and Extended Data Fig. 4c, AUC values of TF regulons of each cell were quantified by SCENIC and projected to UMAP plots.

For Fig. 2d,e, AUC values of TFs inferred from new RNAs were obtained and then subjected to a two-sided Wilcoxon rank-sum test to assess the significance of the difference in TF activity. TFs with a fold change of mean AUC value > 1.5 and an adjusted  $P$  value < 0.05 (Bonferroni corrected) were considered differentially regulated after KCl stimulation in at least one cell type. For Fig. 5c, AUC values of TFs inferred from new or old RNAs were obtained and then subjected to a two-sided Wilcoxon rank-sum test to assess the significance of the difference of TF activity. TFs with a fold change > 1.25 and an adjusted  $P$  value < 0.05 were considered differentially regulated. Notably, we did not identify the regulon activity of Zscan4 in 2C-like cells, potentially due to the lack of Zscan4 motif information in the SCENIC database.

**Data visualization.** All plots were generated using the ggplot2 (v3.3.0), cowplot (v1.0.0) and pheatmap (v1.0.12) packages in R (v3.5.1). In the box plots, the boxes display the median (center line) and interquartile range (from the 25th to 75th percentile), the whiskers represent 1.5 times the interquartile range and the circles represent outliers. In the violin plots, the gray line on each side is a kernel density estimation to show the distribution shape of the data; wider sections of the plot represent a higher probability, while the thinner sections represent a lower probability.

**Statistics.** Statistical analyses were performed using R. Statistical details for each experiment are also provided in the figure legends.

**Reporting Summary.** Further information on research design is available in the Nature Research Reporting Summary linked to this article.

## Data availability

All sequencing data associated with this study have been deposited in the Gene Expression Omnibus (GEO) database under accession code GSE141851. Source data are provided with this paper.

## Code availability

The analysis source code underlying the final version of this paper are available on the GitHub repository (<https://github.com/wulabupenn/scNT-seq/>).

## References

- Sanjana, N. E., Shalem, O. & Zhang, F. Improved vectors and genome-wide libraries for CRISPR screening. *Nat. Methods* **11**, 783–784 (2014).
- Schutsky, E. K. et al. Nondestructive, base-resolution sequencing of 5-hydroxymethylcytosine using a DNA deaminase. *Nat. Biotechnol.* **36**, 1083–1090 (2018).
- Alles, J. et al. Cell fixation and preservation for droplet-based single-cell transcriptomics. *BMC Biol.* **15**, 44 (2017).
- Chen, J. et al. PBMC fixation and processing for Chromium single-cell RNA sequencing. *J. Transl. Med.* **16**, 198 (2018).
- Butler, A., Hoffman, P., Smibert, P., Papalexi, E. & Satija, R. Integrating single-cell transcriptomic data across different conditions, technologies and species. *Nat. Biotechnol.* **36**, 411–420 (2018).
- McInnes, L., Healy, J. & Melville, J. UMAP: uniform manifold approximation and projection for dimension reduction. Preprint at <https://arxiv.org/abs/1802.03426> (2018).
- Stuart, T. et al. Comprehensive integration of single-cell data. *Cell* **177**, 1888–1902 (2019).
- Jurges, C., Dolken, L. & Erhard, F. Dissecting newly transcribed and old RNA using GRAND-SLAM. *Bioinformatics* **34**, i218–i226 (2018).
- Petukhov, V. et al. DropEst: pipeline for accurate estimation of molecular counts in droplet-based single-cell RNA-seq experiments. *Genome Biol.* **19**, 78 (2018).

## Acknowledgements

We are grateful to all members of the Wu laboratory for helpful discussion. This work was supported by the Penn Epigenetics Institute, the National Human Genome Research Institute (NHGRI; grants R00-HG007982 and R01-HG010646), National Heart Lung and Blood Institute (NHLBI grant DP2-HL142044) and National Cancer Institute (NCI; grant U2C-CA233285 to H.W.). The work of P.G.C. is partially supported by Stand Up To Cancer Convergence 2.0.

## Author contributions

H.W., Q.Q. and P.H. conceived and developed the scNT-seq method. Q.Q. conducted most of the experiments. P.H. performed most of the computational analysis and generated the *Tet*-TKO mESC line. X.Q. contributed to RNA velocity analysis. K.W.G. and P.G.C. contributed to the statistical modeling. Q.Q., P.H. and H.W. analyzed the results and wrote the manuscript with contributions from all authors.

## Competing interests

The authors declare no competing interests.

## Additional information

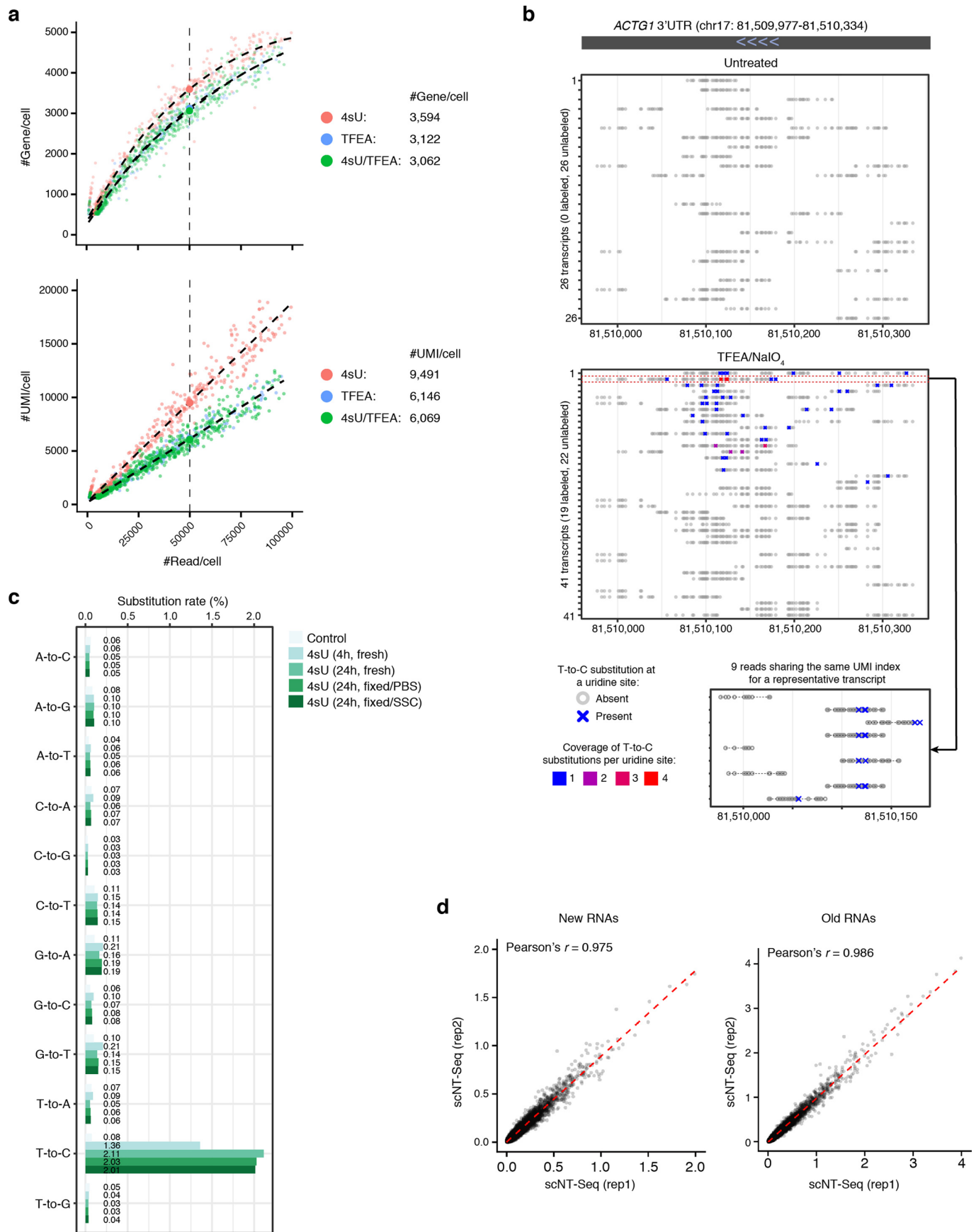
**Extended data** is available for this paper at <https://doi.org/10.1038/s41592-020-0935-4>.

**Supplementary information** is available for this paper at <https://doi.org/10.1038/s41592-020-0935-4>.

**Correspondence and requests for materials** should be addressed to H.W.

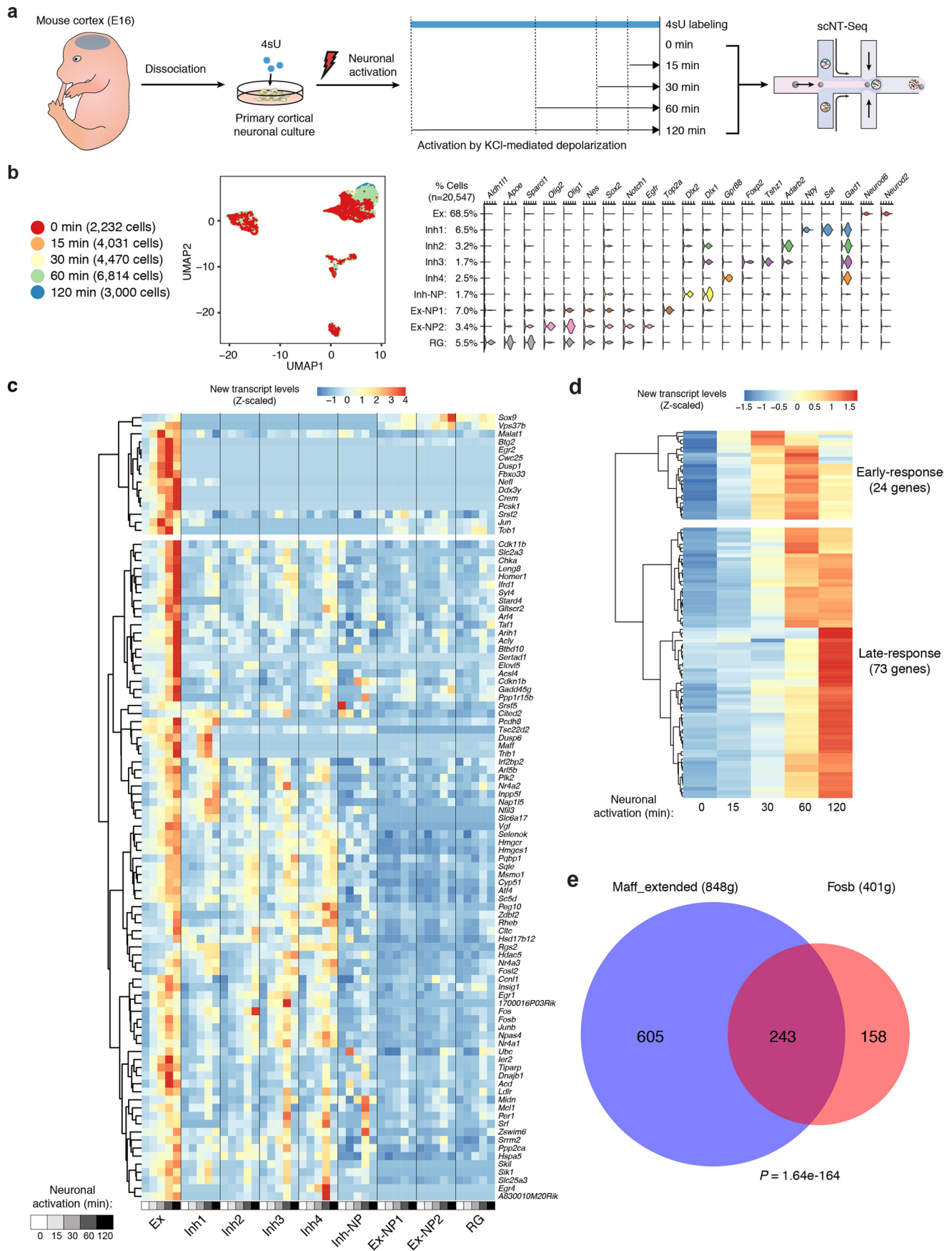
**Peer review information** Lei Tang was the primary editor on this article and managed its editorial process and peer review in collaboration with the rest of the editorial team.

**Reprints and permissions information** is available at [www.nature.com/reprints](http://www.nature.com/reprints).



Extended Data Fig. 1 | See next page for caption.

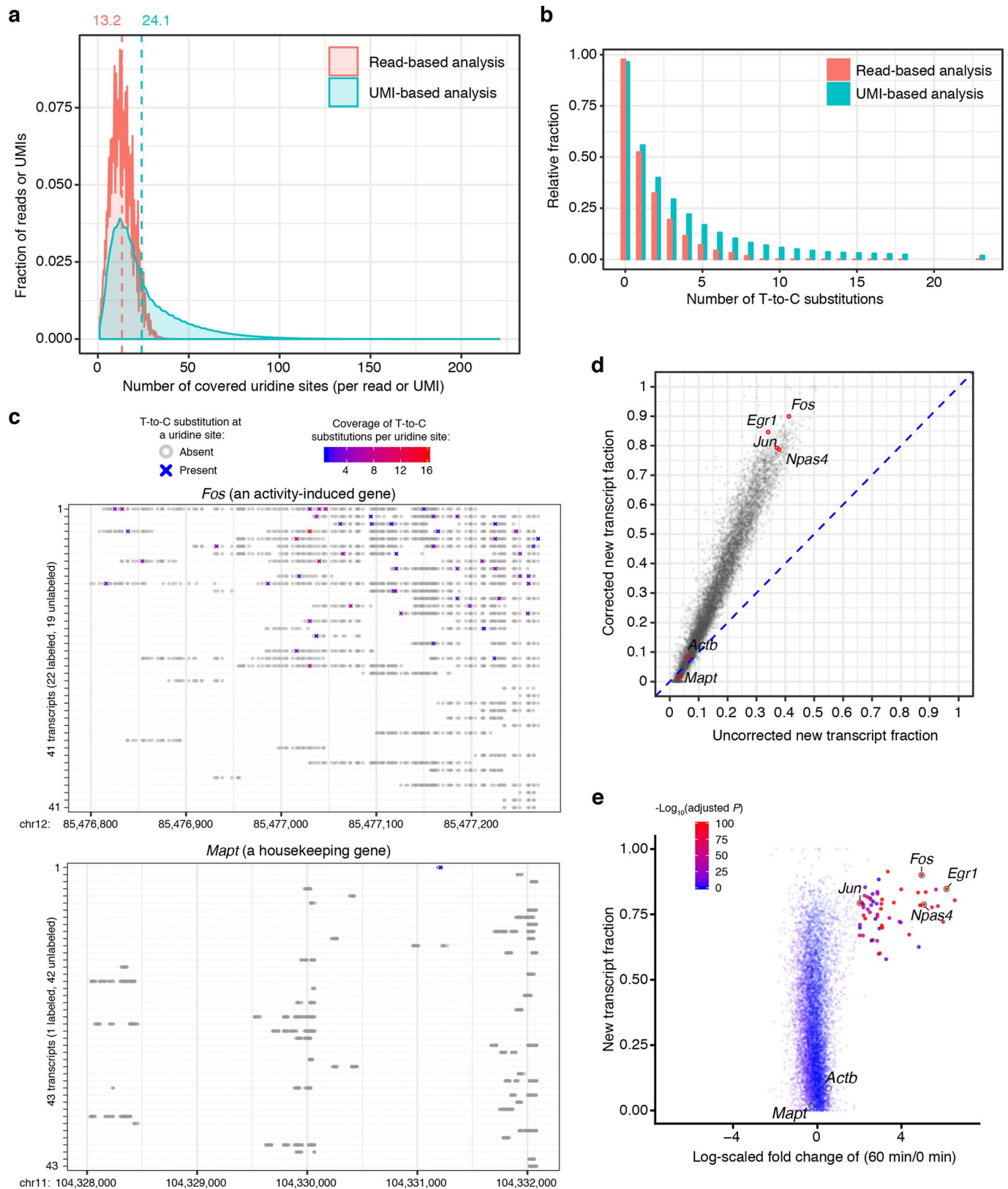
**Extended Data Fig. 1 | Performance and quality control analyses of scNT-seq. a.** Scatterplots showing the number of detected gene per cell (y-axis, upper panel) or UMI per cell (y-axis, lower panel) as a function of aligned reads per cell (x-axis) between 4sU (red, 462 cells), TFEA (blue, 211 cells), and 4sU/TFEA (green, 578 cells) experiments. 4sU, cells labeled with 4sU (100  $\mu$ M, 4 hours (h)). TFEA, beads treated with TFEA/NaIO<sub>4</sub> chemical reaction. 4sU/TFEA, cells labeled with 4sU and beads treated with TFEA/NaIO<sub>4</sub> chemical reaction. The fitted lines of different experiments were shown. The estimated numbers of gene or UMI detected per cell at matching sequencing depth (50,000 aligned read per cell) are shown on the right. **b.** Shown are all transcripts (with unique UMIs) for the *ACTG1* gene from one untreated control K562 cell (upper panel) and one TFEA/NaIO<sub>4</sub>-treated cell (lower panel). Grey circles denote uridine sites without T-to-C substitution, and "X"s denote sites with T-to-C substitutions. The read coverage for each T-to-C substitution is color-scaled. All 9 sequencing reads of the 2nd UMI (in red box) from the TFEA/NaIO<sub>4</sub>-treated cell are highlighted below. **c.** Bar plot showing nucleotide substitution rates in mESCs with different labeling parameters (100  $\mu$ M 4sU for 4 h or 200  $\mu$ M 4sU for 24 h) and sample processing methods (freshly isolated versus methanol fixation followed by cyro-preservation and rehydration with two different rehydration buffers: PBS-based versus SSC-based). A sample (100  $\mu$ M 4sU for 4 h) that was not treated with TFEA/NaIO<sub>4</sub> served as the control. **d.** Scatterplots showing Pearson's correlation between two biologically independent replicates of mESCs (rep1: 427 cells and rep2: 733 cells). The expression levels of new (n = 10,925 genes) and old (n = 14,496 genes) transcripts were quantified as natural log transformation of (TP10K + 1).



Extended Data Fig. 2 | See next page for caption.

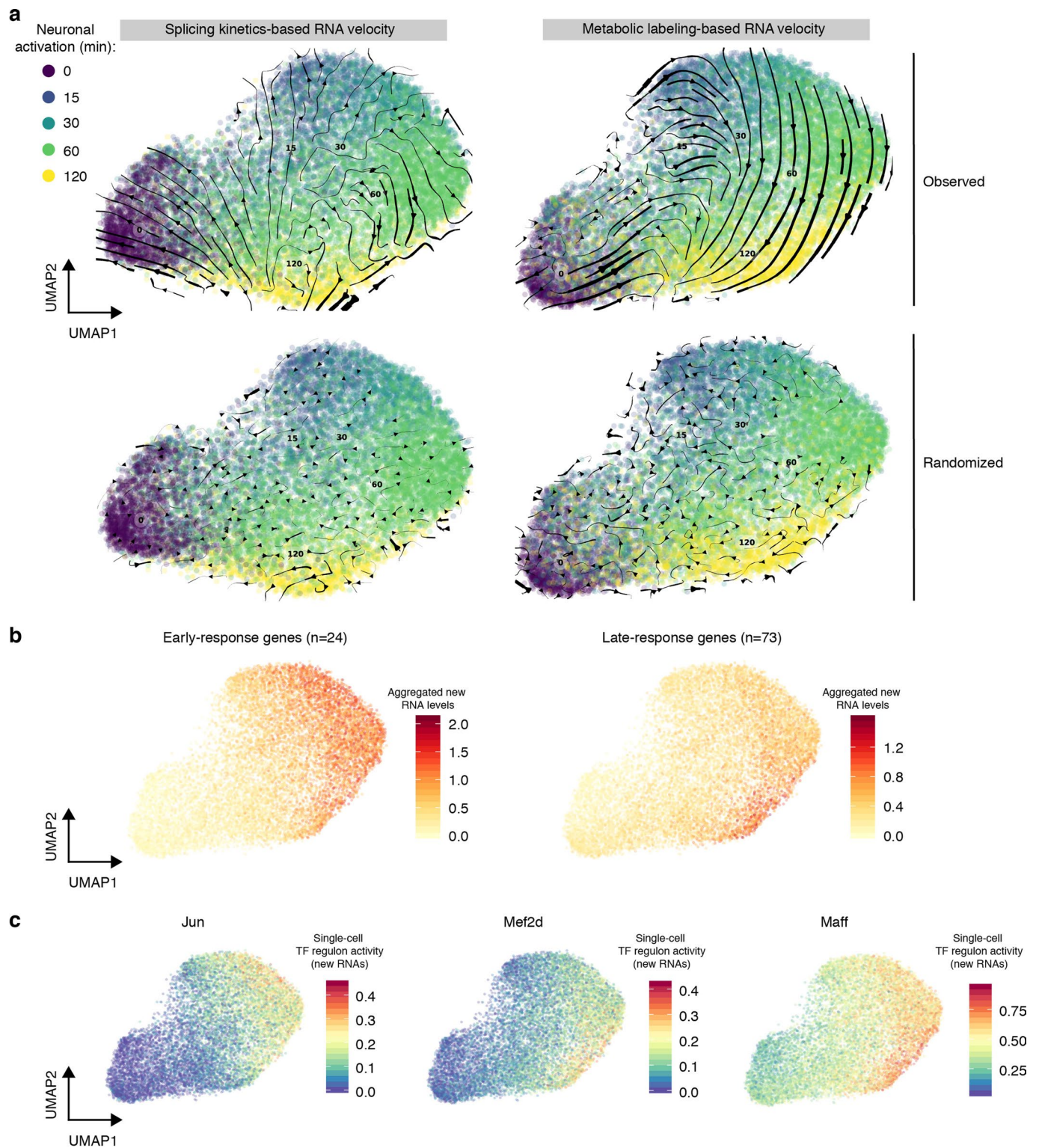
**Extended Data Fig. 2 | Cell-type clustering and analysis of activity-dependent gene expression programs in mouse cortical neuronal cultures. a.**

Experimental scheme of characterizing neuronal activation in primary mouse cortical cultures with scNT-seq. Cells were treated with KCl from 15 min to 120 min. Cells from all treatment conditions were labeled with 4sU for 2 h before harvest for scNT-seq. **b.** Left, UMAP plot for 20,547 cells from mouse cortical cultures (the same UMAP plot in Fig. 2a). The cells are colored by different time points of neuronal activation. Right, violin plot showing the distribution of total RNA levels for representative cell-type specific marker genes. **c.** Clustered heat map showing new RNA levels (z-scaled natural log transformation of (TP10K + 1)) of neuronal activity induced genes across different cell-types. **d.** Clustered heat map showing new RNA levels (z-scaled natural log transformation of (TP10K + 1)) of early- and late-response genes in excitatory neurons with different durations of KCl stimulation. 97 significantly induced genes were clustered into two groups (early- and late-response). The expression levels of early- and late-response genes are in Supplementary Table 2. **e.** Venn diagram showing a significant overlap between Maff and Fosb regulon targets (243 genes,  $P$ -value =  $1.64 \times 10^{-164}$ , Two-sided Fisher's exact test).

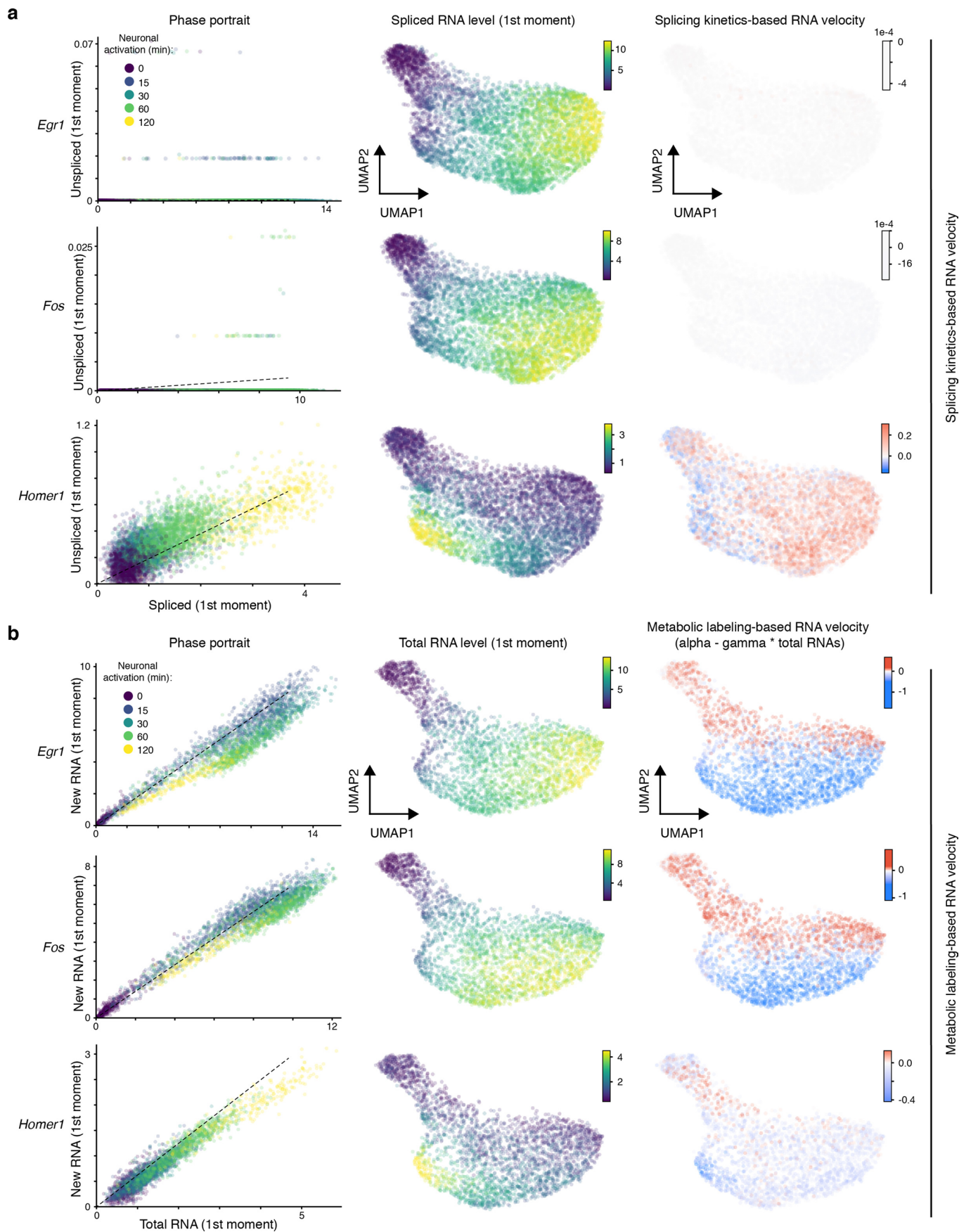


Extended Data Fig. 3 | See next page for caption.

**Extended Data Fig. 3 | UMI-based statistical correction of newly-transcribed RNA fraction.** **a.** Density plot showing the distribution of number of covered uridine sites per read (60 bp) or per UMI (UMI-linked transcript) in excitatory neurons with 60 min of KCl stimulation. **b.** Bar plot of the number of T-to-C substitutions per read (60 bp) or UMI. Shown is the analysis of excitatory neurons with 60 min of KCl stimulation. **c.** Shown are all unique transcripts (with unique UMIs) of the *Fos* (an activity-induced gene) and *Mapt* (a slow turnover housekeeping gene) from a single excitatory neuron with 60 min of KCl stimulation. Grey circles represent uridines without T-to-C conversion, while crosses ("X"s) denote uridines with T-to-C substitution in at least one read. The read coverage for each T-to-C substitution is color-scaled. **d.** Comparison of uncorrected and statistically corrected new RNA levels of each detected gene ( $n=9,082$  genes) in excitatory neurons (with 60 min of KCl stimulation). Four representative activity-induced genes (*Fos*, *Jun*, *Egr1*, and *Npas4*) and two housekeeping genes (*Mapt* and *Actb*) are highlighted with red circles. **e.** Scatter plot showing the new transcript fraction (over total RNAs; y-axis) of excitatory neurons with 60 min of KCl stimulation as a function of differential gene expression (between 60 min and 0 min of KCl stimulation; x-axis). Two-sided Wilcoxon rank sum test was used to assess significance of the difference, and the  $P$ -value was adjusted by Bonferroni correction. Genes were color-coded by statistical significance of differential gene expression. The fraction of new transcripts, expression fold-change, and adjusted  $P$ -value of each gene are in **Source Data Extended Data Fig. 3**.

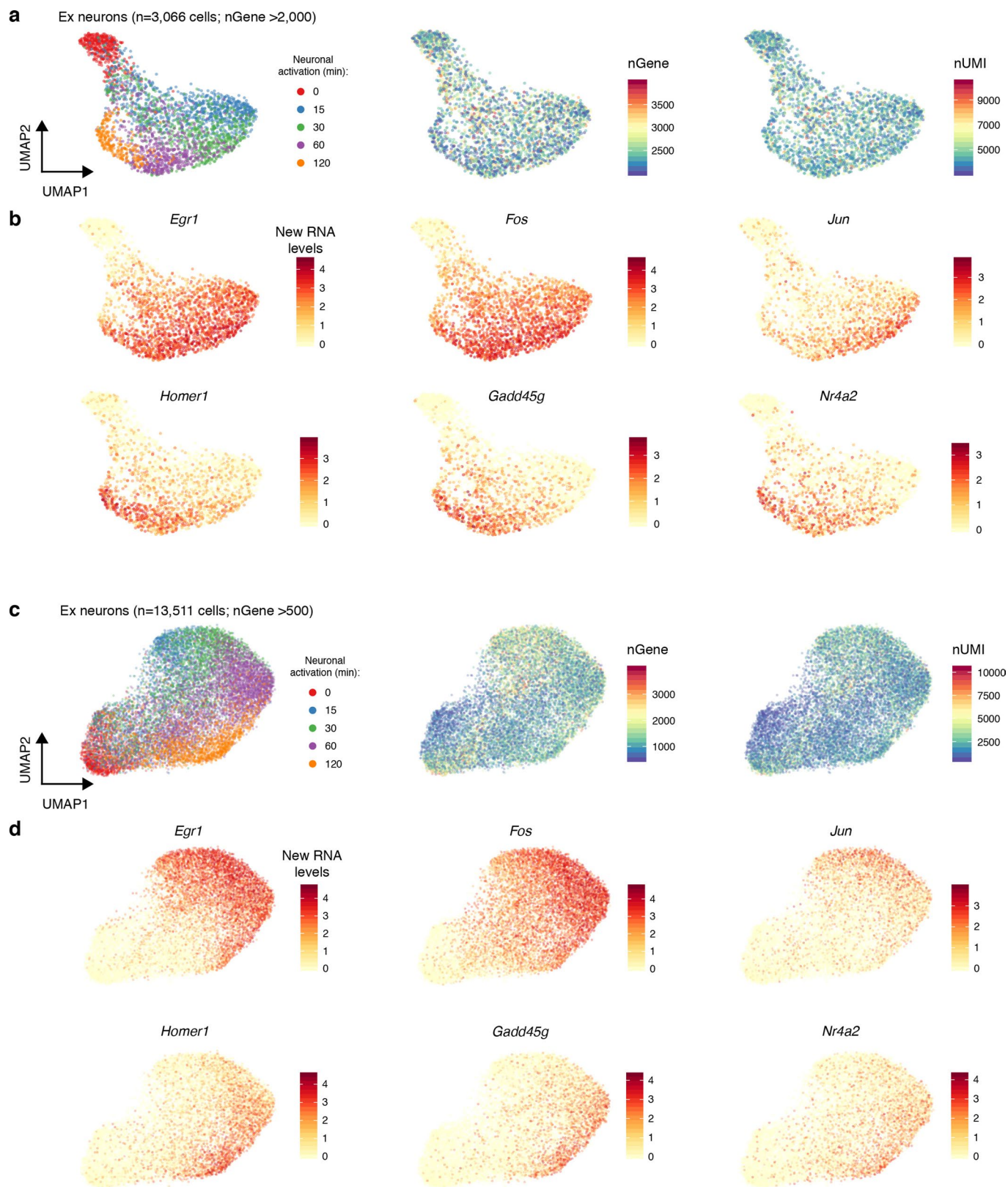


**Extended Data Fig. 4 | scNT-seq enables metabolic labeling-based time-resolved RNA velocity in excitatory neurons.** **a.** UMAP visualization of excitatory neurons (13,511 cells, with >500 genes detected per cell) that were characterized by standard splicing kinetics-based (left) or metabolic labeling based RNA velocity (right) analyses. Cells are color-coded by time points. The streamlines indicate the integration paths that connect local projections from the observed state to extrapolated future state. The thickness of streamline indicates the magnitude of velocity. UMAP plots in lower panels (same as upper panels) show randomized velocity controls for splicing (left) or metabolic labeling (right) based RNA velocity. Permutation of velocity flows was performed by shuffling velocity for genes in each cell and then randomly flipping the sign of shuffled velocity values. **b.** UMAP (same as right of **a**) visualization of Ex neurons colored by the average new RNA expression level (natural log transformation of  $(TP10K + 1)$ ) of 24 early- (left) or 73 late-response (right) genes. **c.** UMAP (same as right of **a**) showing Ex neurons colored by the regulon activity of three representative TFs (Jun, Mef2d, and Maff).

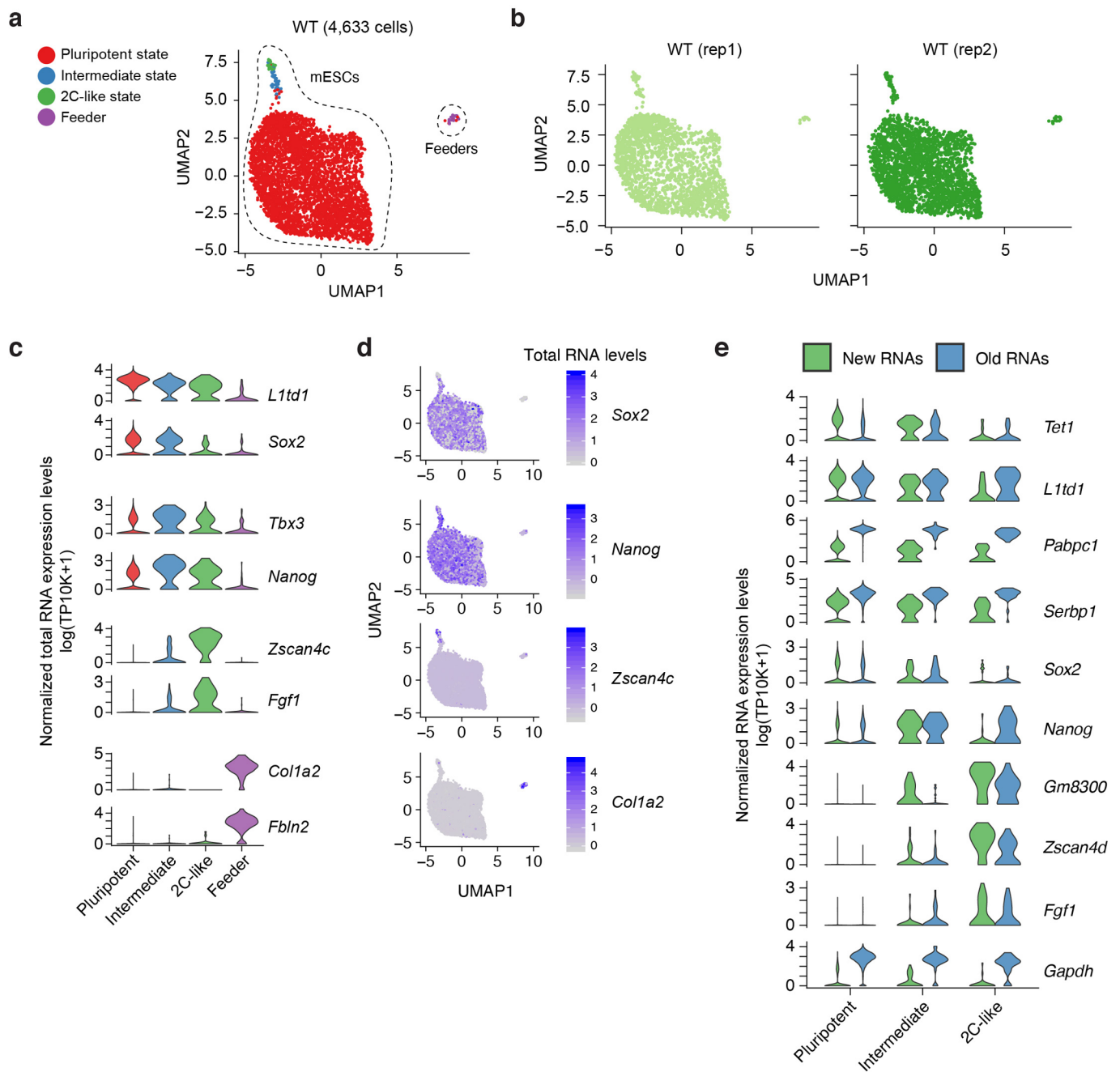


Extended Data Fig. 5 | See next page for caption.

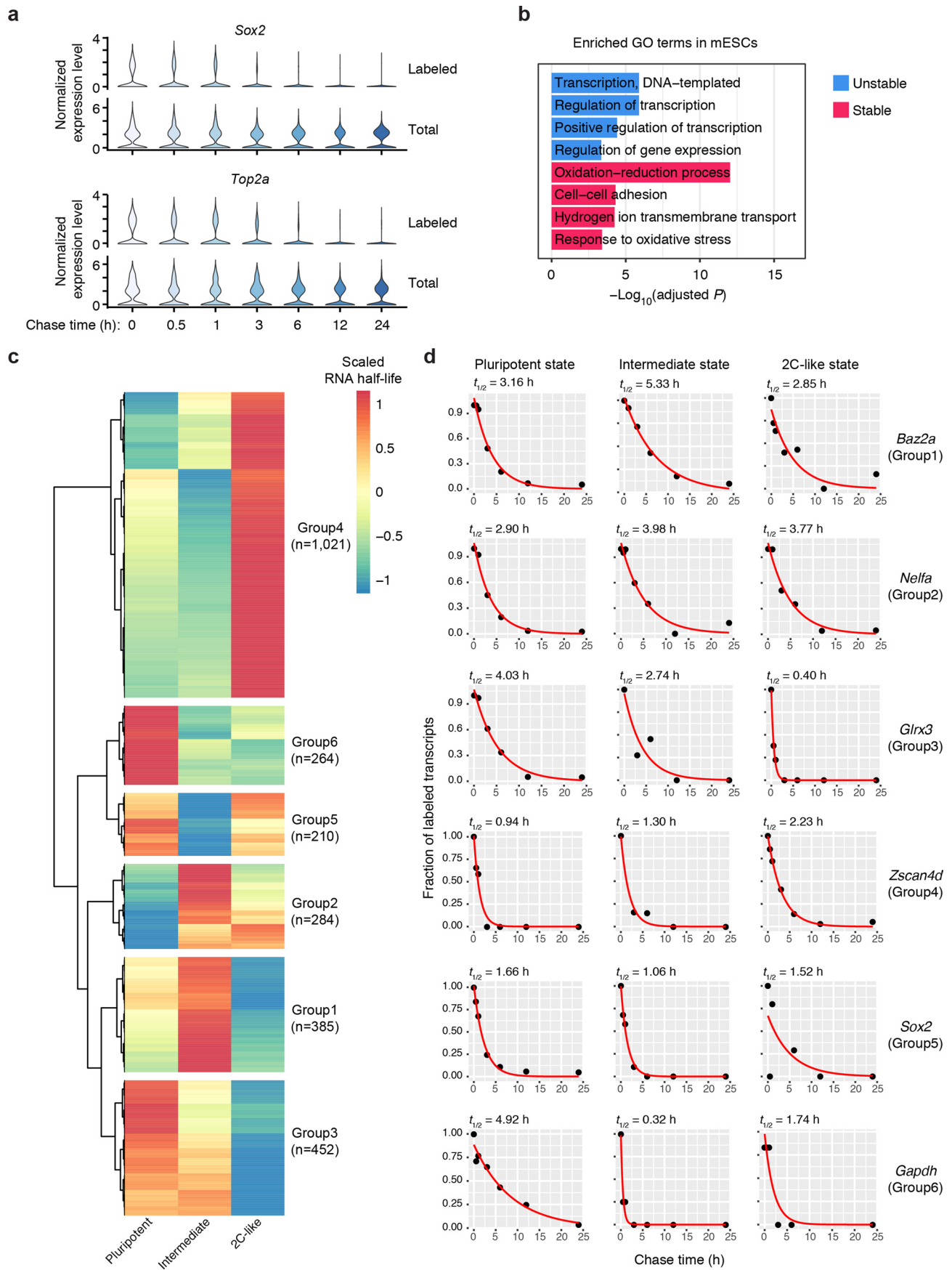
**Extended Data Fig. 5 | Comparison of splicing-based and metabolic labeling-based RNA velocity analysis methods.** The excitatory neurons ( $n=3,066$  cells, with  $>2,000$  genes detected per cell) were analyzed by either splicing kinetics-based **a**, or metabolic labeling-based **b**, RNA velocity. Shown are the phase portraits (left), UMAP plots colored by smoothed spliced (in **a**) or total (in **b**) RNA level based on local averaging (middle), and RNA velocity values (right) of three representative activity-induced genes (*Egr1*, *Fos* and *Homer1*).



**Extended Data Fig. 6 | Quality control for metabolic labeling based RNA velocity analysis.** **a.** UMAP (as in right panels of Fig. 3a) visualization of high-quality Ex neurons (3,066 cells, >2,000 genes detected per cell) colored by time points (left), number of gene detected (middle), and number of UMI detected per cell (right). **b.** UMAP (as in right panels of Fig. 3a) visualization of high-quality Ex neurons colored by the new RNA levels (natural log transformation of  $(TP10K + 1)$ ) of six representative genes, including three early-response genes (*Egr1*, *Fos*, *Jun*) and three late-response genes (*Homer1*, *Gadd45g*, *Nr4a2*). **c.** UMAP (as in right panels of Extended Data Fig. 4a) visualization of all Ex neurons (13,511 cells, >500 genes detected per cell) colored by time points (left), number of gene detected (middle), and number of UMI detected per cell (right). **d.** UMAP (as in right panels of Extended Data Fig. 4a) visualization of all Ex neurons colored by the new RNA levels (natural log transformation of  $(TP10K + 1)$ ) of six representative genes (same as in **b**).

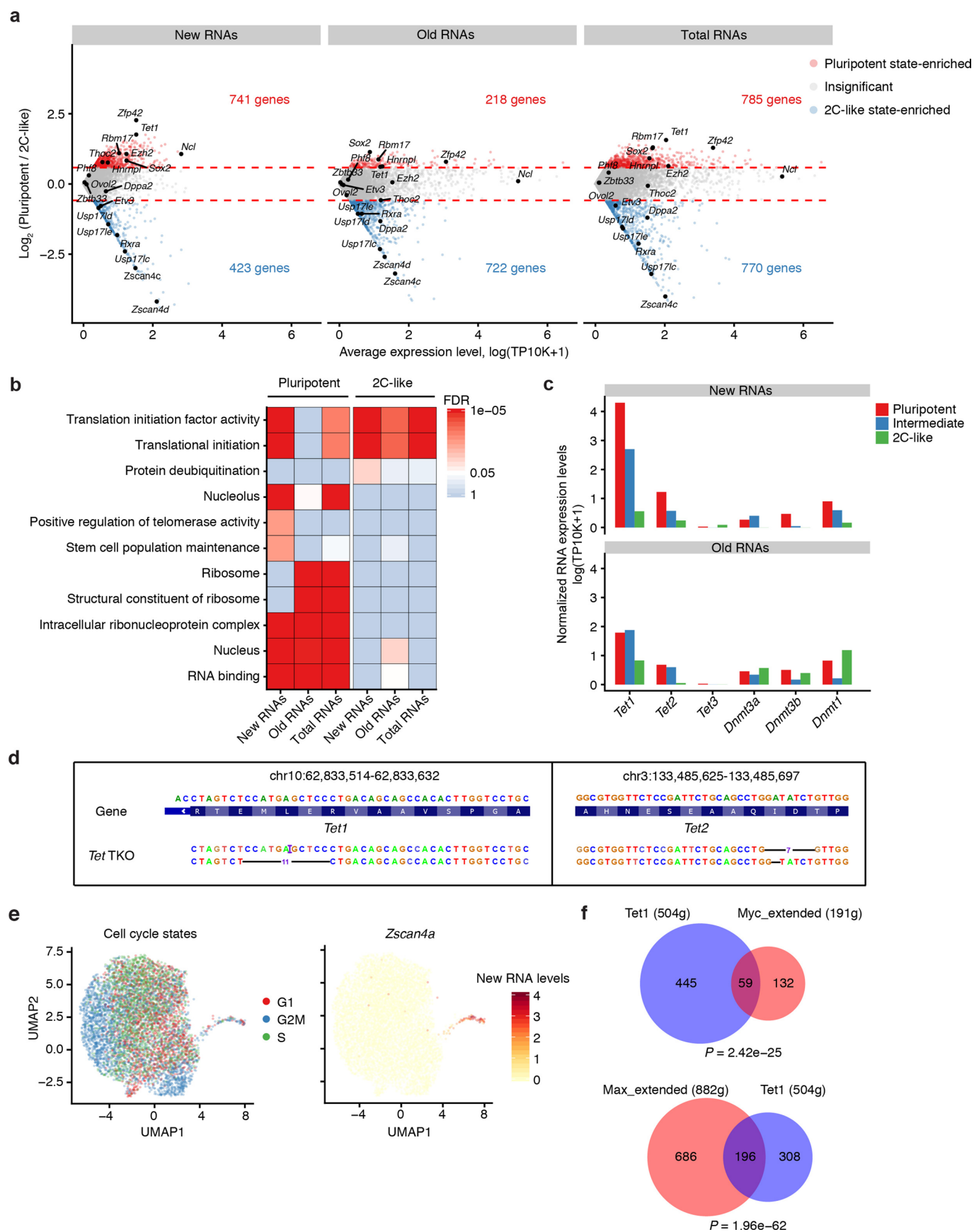


**Extended Data Fig. 7 | scNT-seq reveals different stem cell states in mESC cultures.** **a**. UMAP visualization of 4,633 WT cells (from two biological replicates) colored by different cell-types or cell-states. Feeders are contaminating mouse embryonic fibroblasts. **b**. UMAP visualization of two biological replicates in **(a)**. **c**. Violin plots showing total RNA levels (natural log transformation of  $(\text{TP10K} + 1)$ ) of representative marker genes for feeders or specific stem cell states. **d**. UMAP (same as in **(a)**) visualization of cells colored by total RNA levels (natural log transformation of  $(\text{TP10K} + 1)$ ) of four representative marker genes. **e**. Violin plots showing both new and old RNA levels (natural log transformation of  $(\text{TP10K} + 1)$ ) of selected genes across three stem cell states.



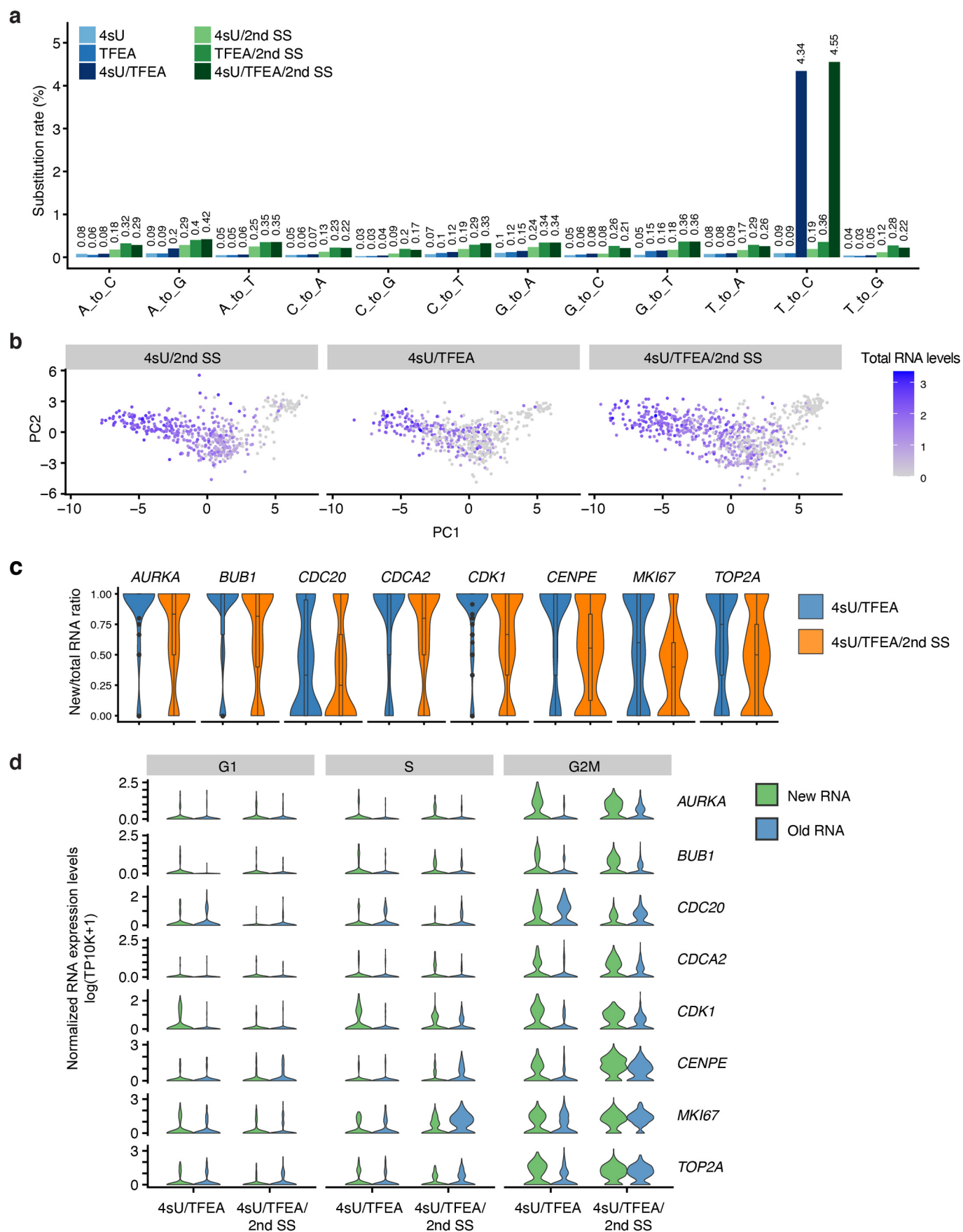
Extended Data Fig. 8 | See next page for caption.

**Extended Data Fig. 8 | Pulse-chase scNT-seq reveals state-specific mRNA half-life.** **a.** Violin plots showing levels of labeled and total transcripts of two representative genes (*Sox2* and *Top2a*) during pulse-chase assay. The expression level is measured in natural log transformation of  $(TP10K + 1)$ . **b.** Enrichment analysis of GO terms within stable (top 10% genes with longest half-lives) and unstable genes (top 10% genes with shortest half-life) in pluripotent state mESCs. Enrichment analysis was performed via a one-sided hypergeometric test.  $P$ -value was then corrected by FDR. The  $P$ -values of GO terms are in **Source Data Extended Data Fig. 8**. **c.** Clustered heat map showing the mRNA half-life of 2,616 genes across three stem cell states. These genes are clustered to six groups based on the scaled RNA half-lives in three cell states. The state-specific half-lives are in Supplementary Table 4. **d.** Shown are mRNA decay curves of representative genes from each group. The fraction of labeled transcripts was calculated for each time point and normalized to chase (0 h), then fit to a single-exponential decay model to derive RNA half-lives ( $t_{1/2}$ ).



Extended Data Fig. 9 | See next page for caption.

**Extended Data Fig. 9 | scNT-seq analysis of the pluripotent-to-2C transition in mESCs.** **a.** Scatter MA-plot showing differential expression of new, old, and total RNAs between pluripotent and 2C-like states. Dashed line denotes 1.5-fold change between states. **b.** Heat map showing enriched GO terms for state-specific genes. Significance of enrichment (FDR) is scaled by colors. Enrichment analysis was performed using a one-sided hypergeometric test.  $P$ -value was then corrected by FDR. The exact  $P$ -values of GO terms are in **Source Data Extended Data Fig. 9**. **c.** Normalized new and old RNA levels (natural log transformation of  $(TP10K + 1)$ ) of major DNA methylation regulators across three stem cell states. **d.** Validation of genotypes of the *Tet1* (-11bp/+1bp) and *Tet2* (-7bp/-1bp) genes in *Tet*-TKO cells by aligning scNT-seq reads to the CRISPR-Cas9 genome editing sites. **e.** UMAP visualization (same as in Fig. 5d) of mESCs colored by cell-cycle states (left) or the new RNA level (natural log transformation of  $(TP10K + 1)$ ) of *Zscan4a* (right). **f.** Venn diagrams showing significant overlap between *Tet1* and Myc regulon target genes (upper) ( $P$ -value =  $2.42 \times 10^{-25}$ , two-sided Fisher's exact test), and between *Tet1* and Max regulon target genes (lower) ( $P$ -value =  $1.96 \times 10^{-62}$ , two-sided Fisher's exact test).



Extended Data Fig. 10 | See next page for caption.

**Extended Data Fig. 10 | Benchmarking the 2nd SS scNT-seq protocol in human K562 cells.** **a.** Bar plot showing nucleotide substitution rates in K562 cells analyzed with different experimental protocols. 4sU, metabolic labeling with 4sU (100  $\mu$ M, 4 h); TFEA, on-bead TFEA/ $\text{NaIO}_4$  chemical reaction; 2nd SS, second strand synthesis. **b.** PCA plots showing K562 cells colored by the total RNA level of the *TOP2A* gene (natural log transformation of  $(\text{TP10K} + 1)$ ) in three experimental protocols (same as in Fig. 6d). **c.** Violin plots showing the new-to-total RNA ratios of 8 representative cell-cycle genes in datasets generated by 2<sup>nd</sup> SS (4sU/TFEA/2<sup>nd</sup> SS,  $n = 795$  cells) or standard (4sU/TFEA,  $n = 533$  cell) scNT-seq protocols. See 'Data visualization' in the Methods for definitions of box-plot elements. **d.** Same as in **c** but showing new and old RNA levels (natural log transformation of  $(\text{TP10K} + 1)$ ) in three cell-cycle states (G1/S/G2M).

## Reporting Summary

Nature Research wishes to improve the reproducibility of the work that we publish. This form provides structure for consistency and transparency in reporting. For further information on Nature Research policies, see [Authors & Referees](#) and the [Editorial Policy Checklist](#).

### Statistics

For all statistical analyses, confirm that the following items are present in the figure legend, table legend, main text, or Methods section.

n/a Confirmed

- The exact sample size ( $n$ ) for each experimental group/condition, given as a discrete number and unit of measurement
- A statement on whether measurements were taken from distinct samples or whether the same sample was measured repeatedly
- The statistical test(s) used AND whether they are one- or two-sided  
*Only common tests should be described solely by name; describe more complex techniques in the Methods section.*
- A description of all covariates tested
- A description of any assumptions or corrections, such as tests of normality and adjustment for multiple comparisons
- A full description of the statistical parameters including central tendency (e.g. means) or other basic estimates (e.g. regression coefficient) AND variation (e.g. standard deviation) or associated estimates of uncertainty (e.g. confidence intervals)
- For null hypothesis testing, the test statistic (e.g.  $F$ ,  $t$ ,  $r$ ) with confidence intervals, effect sizes, degrees of freedom and  $P$  value noted  
*Give  $P$  values as exact values whenever suitable.*
- For Bayesian analysis, information on the choice of priors and Markov chain Monte Carlo settings
- For hierarchical and complex designs, identification of the appropriate level for tests and full reporting of outcomes
- Estimates of effect sizes (e.g. Cohen's  $d$ , Pearson's  $r$ ), indicating how they were calculated

*Our web collection on [statistics for biologists](#) contains articles on many of the points above.*

### Software and code

Policy information about [availability of computer code](#)

Data collection

No software was used for data collection.

Data analysis

STAR (version 2.5.2a), sam2tsv (version ec2c2364), Drop-Seq analysis pipeline (version 1.1.2). Seurat (version 2.3.4, 3.0.0 and 3.1.4), dropEst (version 0.8.5), SCENIC (version 1.1.2.2), dynamo (<https://github.com/aristoteleo/dynamo-release>, commit:9871d78), R (version 3.5.1), R packages: ggplot2 (version 3.3.0), cowplot (version 1.0.0), dplyr (version 0.8.5), tidyr (version 1.0.2), reshape2 (version 1.4.3), pheatmap (version 1.0.12), RColorBrewer (version 1.1.2), MASS (version 7.3.51.5), viridis (version 0.5.1). All scripts for figure generation are available at <https://github.com/wulabupenn/scNT-seq>.

For manuscripts utilizing custom algorithms or software that are central to the research but not yet described in published literature, software must be made available to editors/reviewers. We strongly encourage code deposition in a community repository (e.g. GitHub). See the Nature Research [guidelines for submitting code & software](#) for further information.

### Data

Policy information about [availability of data](#)

All manuscripts must include a [data availability statement](#). This statement should provide the following information, where applicable:

- Accession codes, unique identifiers, or web links for publicly available datasets
- A list of figures that have associated raw data
- A description of any restrictions on data availability

Raw and processed data have been deposited in NCBI Gene Expression Omnibus (GEO) database under accession number GSE141851.

## Field-specific reporting

Please select the one below that is the best fit for your research. If you are not sure, read the appropriate sections before making your selection.

Life sciences       Behavioural & social sciences       Ecological, evolutionary & environmental sciences

For a reference copy of the document with all sections, see [nature.com/documents/nr-reporting-summary-flat.pdf](https://www.nature.com/documents/nr-reporting-summary-flat.pdf)

## Life sciences study design

All studies must disclose on these points even when the disclosure is negative.

Sample size	No statistical procedures were used to select a sample size, but rather, cell numbers typically used in the field were used based on previous studies (Macosko et al, 2015, Cell; Hu et al, 2017, Mol Cell). More than 400 cells were used for two-species mixing experiment. More than 2,000 cells were profiled at each time-point for cortical neuronal culture and mESC pulse-chase experiments. 4,633 WT cells and 2,319 Tet-TKO cells were profiled after 4 hour labeling (from two biological replicates). More than 400 cells were profiled at each of 6 experiments for benchmarking the library complexity of second strand synthesis scNT-Seq protocol.
Data exclusions	Data were not excluded.
Replication	Two biologically independent replicates were included for mESC scNT-Seq experiments (wild-type and Tet-TKO). For mESC pulse-chase experiments, two biologically independent replicates were performed. For other large-scale, high-throughput sequencing datasets, no replication was performed for reasons of cost. Reproducibility of scNT-Seq is accessed in Fig. 5e, Extended Data Fig. 1c and 6b.
Randomization	For estimation the fraction of new transcripts ( $\theta$ ) in each experiment, we randomly sampled 10,000 UMIs to estimate global substitution probabilities $p$ and $q$ based on the binomial mixture model. For PCA analysis of new RNAs, old RNAs, total RNAs and new-to-total RNA ratios, 200 excitatory neurons or non-neuronal cells were randomly sampled from each of two time points. No other randomization strategies were applied.
Blinding	Not applied. Blinding was not relevant since sample identities were encoded into experiment design, and then subjected to scNT-Seq analysis.

## Reporting for specific materials, systems and methods

We require information from authors about some types of materials, experimental systems and methods used in many studies. Here, indicate whether each material, system or method listed is relevant to your study. If you are not sure if a list item applies to your research, read the appropriate section before selecting a response.

### Materials & experimental systems

n/a	Involved in the study
<input checked="" type="checkbox"/>	<input type="checkbox"/> Antibodies
<input type="checkbox"/>	<input checked="" type="checkbox"/> Eukaryotic cell lines
<input checked="" type="checkbox"/>	<input type="checkbox"/> Palaeontology
<input type="checkbox"/>	<input checked="" type="checkbox"/> Animals and other organisms
<input checked="" type="checkbox"/>	<input type="checkbox"/> Human research participants
<input checked="" type="checkbox"/>	<input type="checkbox"/> Clinical data

### Methods

n/a	Involved in the study
<input checked="" type="checkbox"/>	<input type="checkbox"/> ChIP-seq
<input checked="" type="checkbox"/>	<input type="checkbox"/> Flow cytometry
<input checked="" type="checkbox"/>	<input type="checkbox"/> MRI-based neuroimaging

## Eukaryotic cell lines

Policy information about [cell lines](#)

Cell line source(s)	K562 (ATCC, CCL-243) and wild-type mESC line (J1, ATCC, SCRC-1010) were originally purchased from ATCC. Tet-TKO mESC (J1) line was derived in house by CRISPR-Cas9 genome edited using previously validated sgRNAs (Wang et al, Cell, 2013). The Tet-TKO mESC line was verified as noted below.
Authentication	Genotypes of Tet-TKO mESCs (J1) were verified by both Sanger sequencing and single-cell RNA-seq at Tet1/2/3 loci. The lack of 5-hydroxymethylcytosine (5hmC) was confirmed by mass spectrometry as previously described (Schutsky et al, Nat Biotech, 2018). K562 (ATCC, CCL-243) and wild-type mESC (J1 line, ATCC, SCRC-1010) were originally obtained from ATCC and no additional authentication was performed.
Mycoplasma contamination	Not tested.
Commonly misidentified lines (See <a href="#">ICLAC</a> register)	No commonly misidentified cell lines were used.

## Animals and other organisms

---

Policy information about [studies involving animals](#); [ARRIVE guidelines](#) recommended for reporting animal research

Laboratory animals

Embryonic day 16 (E16) C57BL/6 embryos of mixed sex (Charles River).

Wild animals

This study did not involve wild animals.

Field-collected samples

This study did not involve field-collected samples.

Ethics oversight

Experiments were conducted in accordance with the ethical guidelines of the National Institutes of Health and with the approval of the Institutional Animal Care and Use Committee of the University of Pennsylvania. Animals were solely used for collection of material, and no animal experiments were performed.

Note that full information on the approval of the study protocol must also be provided in the manuscript.